Published in final edited form as:

Cell Rep. 2023 November 28; 42(11): 113440. doi:10.1016/j.celrep.2023.113440.

Functional maturation of the rod bipolar to AII-amacrine cell ribbon synapse in the mouse retina

Mean-Hwan Kim[1,4,7,*], **Paulo Strazza Jr.**[1], **Teresa Puthussery**[2,3], **Owen P. Gross**[1,5], **W. Rowland Taylor**[2,3,6], **Henrique von Gersdorff**[1,2,6,*]

[1]The Vollum Institute, Oregon Health & Science University, Portland, OR 97239, USA

[2]Casey Eye Institute, Oregon Health & Science University, Portland, OR 97239, USA

[3]Herbert Wertheim School of Optometry & Vision Science, Helen Wills Neuroscience Institute, University of California, Berkeley, Berkeley, CA 94720, USA

[4]Allen Institute for Brain Science, Seattle, WA 98109, USA

[5]Department of Physics, Reed College, Portland, OR 97202, USA

[6]Senior author

[7]Lead contact

SUMMARY

Retinal ribbon synapses undergo functional changes after eye opening that remain uncharacterized. Using light-flash stimulation and paired patch-clamp recordings, we examined the maturation of the ribbon synapse between rod bipolar cells (RBCs) and AII-amacrine cells (AII-ACs) after eye opening (postnatal day 14) in the mouse retina at near physiological temperatures. We find that light-evoked excitatory postsynaptic currents (EPSCs) in AII-ACs exhibit a slow sustained component that increases in magnitude with advancing age, whereas a fast transient component remains unchanged. Similarly, paired recordings reveal a dual-component EPSC with a slower sustained component that increases during development, even though the miniature EPSC (mEPSC) amplitude and kinetics do not change significantly. We thus propose that the readily releasable pool of vesicles from RBCs increases after eye opening, and we estimate that a short light flash can evoke the release of ~4,000 vesicles onto a single mature AII-AC.

In brief

*Correspondence: meanhwan@gmail.com (M.-H.K.), vongersd@ohsu.edu (H.v.G.).

AUTHOR CONTRIBUTIONS

Conceptualization, M.-H.K. and H.v.G.; methodology, M.-H.K., H.v.G., T.P., and W.R.T.; software, O.P.G. and P.S. Jr.; formal analysis, M.-H.K., P.S. Jr., T.P., W.R.T., and H.v.G.; investigation, M.-H.K., P.S. Jr., and T.P.; writing – original draft, M.-H.K; writing – review & editing, M.-H.K., T.P., W.R.T., and H.v.G.; supervision, M.-H.K., W.R.T., and H.v.G.; funding acquisition, H.v.G., W.R.T., and T.P.

DECLARATION OF INTERESTS

The authors declare no competing interests.

SUPPLEMENTAL INFORMATION

Supplemental information can be found online at https://doi.org/10.1016/j.celrep.2023.113440.

Kim et al. reveal that rod bipolar cell ribbon synapses undergo significant maturation after eye opening. The spontaneous mEPSC frequency, the dual-component EPSC charge transfer, and the peak amplitude of the slow component of the light-evoked EPSC all increase with age.

Graphical Abstract

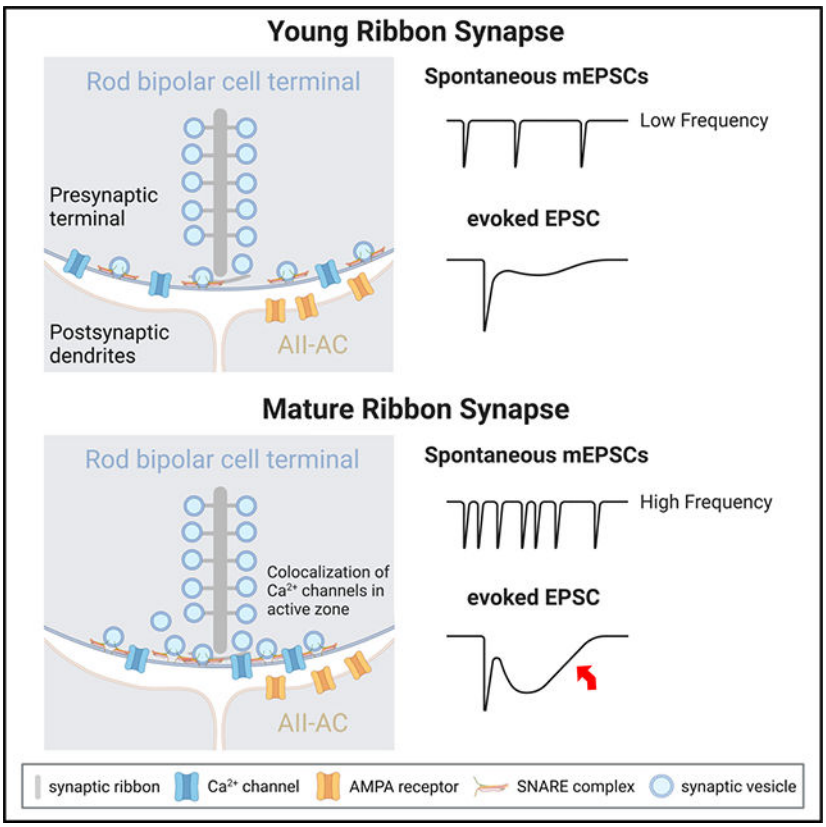

INTRODUCTION

A functional hallmark of sensory ribbon synapses is the indefatigable transfer of information from external inputs.[1] Specifically, in retinal photoreceptors, bipolar cells, and auditory hair cells, synaptic ribbons can encode sustained sensory inputs such as continuous luminance/contrast change or sound intensity/frequency.[2–5] Such synapses have distinct kinetics and durations of transmitter release compared with conventional synapses in the central nervous system.[6,7] Continuous signaling can be achieved by enhanced vesicle replenishment that ensures a constant supply of docked vesicles at the base of the ribbon.[8,9] Importantly, synaptic ribbon architecture changes from postnatal day (P) 12 to P30, with increased ribbon attachment at active zones.[10] Cone photoreceptor Ca^{2+} currents are also smaller at P11 compared with P30.[10] Furthermore, *in vivo* electroretinogram (ERG) studies show that there are dramatic 4- to 9-fold changes in ERG amplitudes and oscillatory potentials from P13 to P30 in rodent retina that probably reflect major changes in rod bipolar cell (RBC) synapses.[11,12] However, it is not known how the RBC-to-AII-amacrine cell (AII-AC) ribbon synapse changes functionally with age.

Vesicle fusion and glutamate release from the ribbon synapses of retinal bipolar cells exhibits fast synchronized and slow sustained release depending upon the time course and amount of Ca^{2+} influx through voltage-gated Ca^{2+} channels.[6,13–15] These dual components of exocytosis, which have been assayed by measuring α-amino-3-hydroxy-5-methyl-4-isoxazolepropionic acid receptor (AMPAR)-mediated excitatory postsynaptic currents (EPSCs), have been observed at bipolar-to-ganglion cell synapses and RBC-to-AII-AC synapses in mouse, goldfish, and zebrafish retina.[16–22] Results from previous studies suggest that the slow EPSC component signals mean luminance.[9,23] The slower component of glutamate release may be due to the delayed fusion of a larger pool of vesicles in the upper rows of the ribbon.[6,24,25] This delayed release of glutamate may also activate a pool of Ca^{2+}-permeable AMPARs (CP-AMPARs) that are not directly adjacent to the ribbon.[15,26,27] Another proposal is that the fast component originates from release sites near the ribbon, where Ca^{2+} channels are clustered, and the slower component originates at non-ribbon release sites that are more distant to the ribbon Ca^{2+} channels.[28–31] A dual-component EPSC also occurs at ribbon synapses between cones and horizontal or bipolar cells with a slow component that is reduced by gap-junction blockers[32,33] but not in mouse RBC terminals.[31]

The origin of the slow EPSC component in AII-ACs thus remains unclear. Moreover, the prominence of the slow component in the evoked EPSCs in AII-AC recordings[19] contrasts with previous analyses that indicated a sometimes small or absent slow component.[9,22,23,25,27,34] One hypothesis is that this difference may be due in part to developmental age and/or temperature, since several previous studies generally used younger animals at room temperature (RT). Therefore, in this study, we investigated how the physiological light response of AII-ACs and the presynaptic release properties of RBC terminals are shaped after eye opening at more physiological temperatures (PTs) in mouse retinal slices.

RESULTS

We first measured light-evoked EPSCs in AII-ACs activated by short light flashes of different durations at two developmental ages: shortly after eye opening (P16) and mature retina (P38). For whole-cell paired recordings between a single RBC and an AII-AC, we used young (P14–P20 mice) and more mature retina (P30–P44 mice). These groups are referred to as “young” and “mature,” respectively.

Characteristics of light-evoked EPSCs in AII-Acs

To investigate the kinetics of RBC ribbon-mediated exocytosis during physiological stimulation, we measured light-evoked EPSCs in AII-ACs under whole-cell voltage clamp while holding the cells at the chloride reversal potential (−70 mV). AII-ACs were targeted for recording based on the presence of a thick primary dendrite (see morphology in Figures 2D, 3A, and 3B)[26,35] and the characteristic shape and location of the cell bodies adjacent to the inner plexiform layer border. Intensity-response relations for EPSCs were measured over a range of light intensities, spaced approximately logarithmically between 0.17 and 340 photons/μm^2. Light-flash intensity was adjusted by changing the duration of the flashes up to a maximum of 20 ms.

Light-evoked EPSCs displayed two kinetic components in both young (P16) and mature (P38) retinas. A fast component reached a negative peak in less than 100 ms followed by an inflection, after which the EPSC reached a second negative peak (Figures 1A–1C and 1F). The two components were evident in responses from individual cells (Figures 1A–1C, left column) and in the group averages (Figures 1A–1C, middle and right). The magnitudes of the two components as a function of the stimulus strength were estimated by measuring the peak inward current at fixed time points (red lines, Figures 1A–1C) and total charge early and late in the EPSCs. The early charge (Q_{Fast}) and late charge (Q_{Slow}) are the areas under the EPSC before and after the blue line in Figures 1A–1C, respectively.

There was no significant difference between young and mature animals in the amplitude of the fast EPSC component (A_{Fast}) or in Q_{Fast} (Figures 1D and 1E, upper graph). The maximum amplitude of the slow component (A_{Slow}) was about 40% smaller in the young animals than in the mature animals (two-way ANOVA, $p = 3.5 \times 10^{-8}$); however, the magnitude of Q_{Slow} was not significantly affected ($p = 0.096$), possibly because the decrease in amplitude was offset by an increase in the duration of the EPSCs in the young animals (see Figure 1H). Analysis of the EPSC charge transfer shows that Q_{Fast} represents less than 10% of the total charge (Figure 1E), indicating that under physiological conditions, the slow temporal component will account for the bulk of synaptic release from the presynaptic RBCs.

We next normalized the amplitudes of the EPSCs to compare the sensitivity of the two components. Two-way ANOVA revealed that the intensity-response relation of A_{Slow} was shifted to lower intensities relative to A_{Fast}. The half-maximal (half-max) light intensities obtained from the fits to the intensity-response relations (black and blue lines, Figure 1D) indicate that A_{Slow} was activated at intensities about 1 log unit lower than A_{Fast} at both developmental time points (Figure 1D; half-max intensities: mature, A_{Fast} 13.4 photons/μm^2, A_{Slow} 1.6 photons/μm^2, $p = 2.6 \times 10^{-8}$; young, A_{Fast} 6.0 photons/μm^2, A_{Slow} 0.7 photons/μm^2, $p = 5.6 \times 10^{-9}$). These data also show that the half-max light intensities were about 2-fold lower in the young animals for both A_{Fast} and A_{Slow} (two-way ANOVA, $p = 0.023$ and 0.025, respectively). Finally, we measured EPSC activation delay and duration as a function of flash intensity (Figures 1F, 1G, and 1H). The activation delay in the young and mature animals was indistinguishable (Figure 1G), while the duration was significantly longer in the young animals (two-way ANOVA, $p = 0.0073$), by about 40% at low intensities, converging to equality at the highest intensities (Figure 1H). Overall, the results point to differential development of the two EPSC components, with A_{Fast} reaching maturity before A_{Slow}.

Depending on the light-adaptation level, AII-ACs can be electrically coupled to one another via gap junctions. Therefore, we considered the possibility that A_{Slow} might represent temporally filtered currents through gap junctions from adjacent AII-ACs. The strength of such coupling is modulated by the light-adaptation state of the retina.[36–39] Under low-scotopic and high-photopic conditions, the AII-AC network is minimally coupled, whereas over the intermediate operating range, the network becomes more extensively coupled. Under our scotopic recording conditions, we did not expect to see strong coupling; nonetheless, we performed experiments in mature AII-ACs in a Cx36-knockout (KO) mouse

to control for potential effects of coupling. If A_{Slow} were due to synaptic current flowing in from adjacent coupled cells, then it should be selectively suppressed in the Cx36-KO animals. However, although the amplitudes of the EPSCs in the CX36-KO retinas were reduced relative to wild-type controls, A_{Fast} and A_{Slow} were equally affected (maximum response reduced by 49% [$p = 6.8 \times 10^{-7}$] and 58% [$p = 3.1 \times 10^{-12}$], respectively). This result indicates that A_{Slow} cannot be simply attributed to gap-junction inputs, consistent with the expectation that coupling between AII-ACs will be weak under our recording conditions.

When coupling is strong, adjacent AII-ACs can contribute a slow component to the light-evoked EPSC that does not reverse at positive voltages,[40,41] because voltage-clamp control through the gap junctions is poor, and therefore, light stimuli will always produce a relative depolarization in gap-junction-connected AII-ACs. As an additional control for contributions from gap junctions, we measured current-voltage (I-V) relations for the net light-evoked EPSCs between −100 and +80 mV in both wild-type and Cx36-KO mice (Figure 2). Contrary to the expectations for a gap-junction-mediated current, the light-evoked EPSCs displayed linear I-V relations and reversed at ~0 mV[19] for both A_{Fast} and A_{Slow} in both the wild-type and the Cx36-KO retinas (Figures 2A–2C). Strong gap-junction connectivity is also expected to reduce the input resistance (R_{input}) of the AII-ACs. We measured the R_{input} in wild-type and KO retinas by fitting a line to the leak current between −100 and −20 mV, and indeed, R_{input} was higher in Cx36-KO mice (Figure 2E). Overall, these results indicate that gap-junction connectivity between AII-ACs is low under our scotopic conditions and that the slow EPSC component cannot simply be attributed to current flow through gap junctions. The dual-component responses seen in the AII-ACs also cannot be attributed to the properties of the photoreceptor inputs to the RBCs, since light-evoked inputs to RBCs under similar recording conditions are characterized by monotonic responses that rise to a single peak without evidence for secondary processes.[42] Moreover, the time to peak of responses in dark-adapted RBCs is similar to that seen for the slow component of the AII-AC EPSCs shown here.[42] Therefore, we hypothesized that their origin lies in the properties of glutamate exocytosis from the RBC synaptic terminals to AII-ACs during postnatal development.

Developmental changes of RBC-driven EPSCs in AII-AC synapses

To directly investigate glutamate exocytosis from single RBCs, we made paired recordings in retinal slices from RBC and AII-AC somas. This allowed us to depolarize a single RBC and measure the resultant evoked EPSCs in an AII-AC at −70 mV. RBCs were targeted by their characteristic soma shape and position adjacent to the outer plexiform layer and their identity was confirmed by morphological examination after filling cells with fluorescent dye during the recordings (Alexa 594 hydrazide for RBC and Alexa 488 hydrazide for AII-AC; Figures 3A and 3B; see also method details in the STAR Methods). During the paired recordings, EPSCs in AII-ACs were evoked by depolarizing the RBC from −70 to −10 mV for 200 ms (Figures 3C and 3D). Remarkably, neither the amplitude nor the time course of the Ca^{2+} currents recorded in the RBCs changed significantly between the young and the mature groups (Figure 3C; amplitude of Ca^{2+} currents, 20.89 ± 2.92 pA for P14–P20, n = 7, and 21.59 ± 2.82 pA for P30–P44, n = 13, p = 0.818).

Depolarization of the RBC evoked an EPSC in the AII-AC that had two components: a fast, transient component and a more delayed, sustained component. These two components have been attributed to synchronous and asynchronous release, which draw upon different pools of synaptic vesicles in the synaptic terminal.[6,27,28] The amplitude of the fast and slow components of the evoked EPSCs in mature (P30–P44) versus young (P14–P20) age groups increased by 145% ($p = 0.1271$) and 201% ($p = 0.0087$), respectively ($n = 11$ for the young group, $n = 19$ for the mature group; Figure 3D). In addition, the onset delay of evoked EPSCs was significantly shorter in the mature age group (1.35 ± 0.06 ms in the young age group, $n = 11$, P14–P20; 1.05 ± 0.04 ms in the mature age group, $n = 19$, P30–P44, $p = 0.005$; Figure 3D, inset). To determine whether there is a developmental switch at a specific time point or whether this change emerges more gradually, we also studied additional ages outside of the two main age groups (P21, P23, and P29). This analysis supports the idea that there is a gradual change in EPSC amplitude during development (Figure S1). This suggests that synaptic transmission at these synapses becomes faster and more robust during development after eye opening.[10]

To understand the mechanisms underlying the developmental change of evoked EPSCs, we also recorded spontaneous miniature EPSCs (mEPSCs) in both age groups (Figure 4) to determine whether the increase in evoked synaptic transmission is due to either (1) an increase in mEPSC quantal size or (2) an increase in the vesicle pool size with the same mEPSC quantal size. Spontaneous mEPSCs were recorded in control conditions and in the presence of 10 μM L-AP4 to completely suppress mGluR6-gated currents and thus reduce the probability of exocytosis resulting from tonic depolarization of RBCs (Figures 4Ai and Aii).[14,43] The mEPSC amplitude distribution in both young and mature groups was well fit by a log-normal distribution function (Figure 4Bi):

$$Y(x) = \frac{A}{X} e^{-\frac{1}{2}\left(\frac{\ln(x/\mu)}{\ln(\sigma)}\right)^2}.$$

The log-normal parameters μ (geometric mean) and σ (skewness) are shown in Table S1. Amplitudes (Figures 4Bi and 4Ci) and frequencies (Figures 4Bii and 4Cii) of mEPSCs were significantly decreased in the presence of 10 μM L-AP4 compared with control.[14,43] However, the mEPSC amplitude and their kinetics were not significantly different between age groups (Figures 4Aii, Ci and S2A; Table S1). Importantly, we observed that the frequency of spontaneous mEPSCs in the presence or absence of L-AP4 increased with age (Figure 4Cii), suggesting significantly more fusion-competent vesicles in mature synapses. To determine whether the mEPSCs in both age groups were univesicular events, we applied 100 μM Cd^{2+} to block Ca^{2+} channels[44,45] in RBC presynaptic terminals in the presence of 10 μM L-AP4. This additional application of 100 μM Cd^{2+} did not significantly change event amplitude, but the event frequency was greatly decreased (Figure S2). This suggests that the mEPSCs in the young and mature age groups in L-AP4 are indeed due to single-vesicle fusion events rather than multivesicular events.

CP-AMPARs are expressed in rodent AII-ACs.[15,27,46,47] Therefore, we tested the possibility that there was selective upregulation of CP-AMPARs during the developmental period

from P19 to P38.[47] We used a selective antagonist of CP-AMPARs, IEM 1460 (IEM: an open channel blocker),[48–50] to determine whether the fractional block of EPSCs in AII-ACs increased during development after eye opening. The antagonist IEM 1460 (60 μM) blocked both fast and slow EPSC components almost completely (8.6% total charge remained after treatment, n = 9, p = 0.0151; Figure S3B). The evoked responses were partially restored after IEM washout (data not shown). However, there was no correlation between developmental age (P19–P38) and fractional block of EPSCs by IEM ($r = -0.0261$, p = 0.9468). This suggests that the proportion of CP-AMPAR expression in AII-ACs is not selectively upregulated after mouse weaning (P19–P20). Thus, CP-AMPARs likely carry the majority of the postsynaptic current in AII-ACs at the developmental time points tested.[51,52]

Temperature significantly changes the kinetics and amount of release from RBCs

Light-evoked responses are more robust near PTs (~32°C–35°C); however, many previous studies were performed at RT (~24°C).[9,13,22,27,43] To examine the temperature dependence of synaptic function, we performed paired recordings at PT and RT. Temperature was initially maintained at PT (gray) and then lowered to RT (red) and raised back to PT (black in Figure 5A) over a 5–10 min period. The results were similar starting at RT and increasing to PT and then decreasing back down (data not shown). Presynaptic Ca^{2+} currents were decreased by 24.4% ± 12.9% (n = 6, p = 0.0057) at RT relative to PT in both young and mature age groups (25.0 ± 4.2 pA in young and 27.1 ± 13.5 pA in mature for PT; Figures 5A and 5D). Standing leak currents were also regulated by temperature; the magnitude of the holding currents decreased reversibly at RT compared with PT (Figure 5A, bottom). The onset delay of the evoked EPSCs was slower at RT than at PT (1.89 ± 0.09 ms at RT, 1.16 ± 0.10 ms at PT, p = 0.0002, n = 8, P17–P34; inset in between Figures 5A and 5B). As expected, the amplitude of the average mEPSC was smaller and the decay kinetics were slower at RT in both young and mature age groups (P17–P40; Figure 5C).[51,53,54] In the mature age group, the average mEPSC amplitudes changed from 16.67 ± 1.00 pA at RT to 19.37 ± 1.12 pA at PT.[43,51] The average charge transfer (fC) was not significantly different at RT (36.17 ± 12.22) compared with PT (32.47 ± 13.05) (p = 0.21, pairwise t test, Figure 5C; see Table S1 for another dataset at PT). The charge transfer of the fast and slow components of the evoked EPSC was significantly larger at PT relative to RT (176% ± 42% for fast [p = 0.146] and 255% ± 25% for slow [p = 0.004] component at PT, total charge [p = 0.011], pairwise t test, n = 8, P17–P40; Figures 5A and 5D). This indicates that the slow component is temperature sensitive and reduced at RT.

The smaller evoked-EPSC amplitudes could result at least in part from the temperature-dependent reduction in the amplitudes of the mEPSCs and also from changes in release probability (Pr). To separate these two effects, we used a deconvolution analysis (see method details in the STAR Methods and Figure S4) to fit the evoked EPSCs based on observed mEPSCs and inferred release rates. When applied to evoked EPSCs recorded at RT and PT, the deconvolution analysis predicts that PT increases the rate of transmitter release (Figures 5A and 5C). The release rates (Figure 5B, top) were integrated and displayed as a cumulative release curve (Figure 5B, bottom) to illustrate the lower overall glutamate release at RT. The initial fast jump in the integral and slower secondary increase matched the fast and slow kinetics of evoked EPSCs shown in Figure 5A. Consistent with the amplitude

analysis, the deconvolution analysis also indicates that the slow release rate was more strongly affected by temperature (arrow in Figure 5B). Therefore, we conclude that the slow component of release likely plays a more prominent role at more PTs. Higher temperature thus increases the overall amount of exocytosis and the kinetics of glutamate release.[53,54]

Desensitization of postsynaptic CP-AMPARs by presynaptic exocytosis

The maximum amplitudes of light-evoked EPSCs were comparable to our depolarization-evoked EPSCs in paired recordings (e.g., compare Figures 1 and 3). However, light-evoked EPSCs arise from the activation of several RBCs,[55,56] while our paired recordings strongly depolarized a single RBC. The equivalent EPSC amplitudes suggest that the individual synapses are being driven much more strongly during the paired recordings. This raises the possibility of quantitative differences in synaptic dynamics during light-evoked (Figures 1 and 2) and depolarization-evoked transmission (Figures 3, 5, and S3). For example, the deconvolution analysis assumes linear summation of mEPSCs and thus discounts the possibility of postsynaptic receptor desensitization or saturation.[57,58] To control for potential effects of AMPAR desensitization, we repeated the deconvolution analysis during application of 50 μM cyclothiazide (CTZ), a blocker of AMPAR desensitization.[6,59–61] CTZ had strong effects in both young (P18) and mature (P30) evoked EPSCs (Figures 6A and 6E). The averaged amplitude of mEPSCs was increased in the presence of 50 μM CTZ in the young but not in the mature age group, and the decay became prolonged in both young and mature age groups (Figures 6B and 6F, insets).[13,27,51] With mEPSCs and evoked EPSCs in the presence of 50 μM CTZ, we were able to perform deconvolution analysis in both age groups. Interestingly, desensitization of evoked EPSCs was weaker in the young compared with the mature age group. We suggest that desensitization was weaker in the young age group due to less glutamate release rather than due to changes in AMPAR composition during development (Figure S3). There was no significant change in presynaptic Ca^{2+} currents that could account for the increased EPSCs in the presence of CTZ (amplitude of Ca^{2+} currents, 19.67 ± 2.60 pA in control, 18.10 ± 1.82 ms in CTZ, P16–P43, $p = 0.19$, $n = 5$).

Deconvolution analysis indicates that the increase in the mEPSC duration was not sufficient to account for the larger evoked EPSCs in the mature age group (Figure 6F, inset). An increase in the release rate was observed in the presence of CTZ, compared with control (black and gray traces compared with red traces shown in Figures 6A, 6E, 6B, and 6F). The deconvolution analysis thus shows evidence of postsynaptic AMPAR desensitization in the later phase of exocytosis in the mature compared with the young age group (paired ensemble average; Figures 6C and 6G). A large increase in glutamate release at mature synapses may explain this increase in AMPAR desensitization. Thus, blocking desensitization with CTZ reveals the actual vesicle release rates during depolarization. Note that even without CTZ our deconvolution analysis still shows the increase in total exocytosed vesicles during development in a grand ensemble average of all paired recordings (Figures 6D and 6H). These results also help us better understand the observed light-evoked EPSC time course in the AII-ACs, which displays a slowly developing secondary peak that is well separated from the initial fast peak (Figures 1 and 2),[19] because the slow sustained component of the light response reflects the aggregate activation of many distinct RBC synapses.

Paired-pulse ratio and presynaptic glutamate transporters

To gain insight into Pr, we next monitored the relationship between the kinetics of presynaptic Ca^{2+} currents and the EPSC amplitude with paired-pulse stimulation (Figure 7A).[6,27] This experiment shows that the paired-pulse ratio is small (<0.5) due to a strong paired-pulse depression (P34; Figure 7A). This suggests a high Pr for strong depolarizing pulses in the mature RBC. Indeed, Jarsky et al.[34] have shown that 1 mM external Ca^{2+} is enough to saturate the EPSC amplitude, again suggesting that Pr is high at 34°C for P30–P40 RBC synapses. Assuming an average of 38 synaptic ribbons per mouse RBC, we estimate that a cluster of Ca^{2+} channels has 27/38 = 0.7 pA/ribbon, given our whole-cell Ca^{2+} current amplitudes at PT for a mature RBC (27.05 ± 13.52 pA; Figure 5). This suggests that maybe six to nine open Ca^{2+} channels per ribbon (with only one or two open at any given moment) are required to trigger the EPSC, assuming a single Ca^{2+} channel current of 0.4 pA[34] and maximal open probability of L-type Ca^{2+} channels of around 0.2–0.3.[62–64] Thus, the multiple ribbon synapses from a mature RBC to a single AII-AC ensure robust and prolonged EPSCs with a relatively small amount of presynaptic Ca^{2+} influx. By contrast, the EPSCs are delayed, dispersed, and reduced in amplitude in young synapses, suggesting that Ca^{2+} nanodomains are not fully formed.[34]

Previous studies reported the expression of glutamate transporters in mammalian RBCs[65–67] and goldfish bipolar cell terminals.[68] Thus, we tested the impact of glutamate transporter activity on the kinetics of EPSCs by applying 100 μM D,L-TBOA, a competitive blocker of glutamate transporters.[17,69] Blocking glutamate transporters did not significantly affect the kinetics of the EPSCs in the AII-ACs,[31] indicating that diffusional processes probably dominate the clearance of transmitter from the synaptic cleft (Figure 7B). In addition, we also noticed a slight increase in steady-state presynaptic Ca^{2+} currents and an increase in EPSC size (Figure 7B, inset). We suggest that (1) presynaptically, an outward transporter-mediated current occurs during the depolarization of the RBC due to a slow sustained exocytosis such that the net size of inward currents in the RBC could be decreased in control, but increased in the presence of D,L-TBOA, and (2) postsynaptically, a reduction in glutamate clearance from the synaptic cleft with D,L-TBOA could perhaps activate more extrasynaptic AMPARs. During these experiments, we noted the presence of a transient outward current component at the onset of the Ca^{2+} current (see arrows and inset in Figure 7B). This initial “notch” current was blocked during D,L-TBOA application,[17,65] suggesting that it resulted mostly from the electrogenic activity of glutamate transporters in the RBC terminals. Consistent with this idea, the size of the notch correlated closely with the size of peak EPSC responses (see inset in Figure 7A). However, since protons are co-transported with glutamate, blocking transporters could also alter cleft pH, perhaps saturating proton binding sites on Ca^{2+} channels or altering pH dynamics.[34,70,71] Interestingly, no initial notch responses were detected on the Ca^{2+} currents in some of the young age group recordings (P15–P17, data not shown), suggesting that presynaptic glutamate transporter location and/or function may be established only after more mature synaptic connections are made or the amount of glutamate release is reduced in young synapses and may not be enough to activate the glutamate transporters. We note that a recent study suggests no significant differences in glutamate transporter expression pattern during development.[72]

DISCUSSION

Our main findings are that (1) the fast component of the light-evoked EPSC has a higher threshold than the slow sustained component; (2) the peak amplitude of the slow component of the light-evoked EPSC increases with age, whereas the fast component remains unchanged; (3) the mEPSC frequency increases greatly with age, but amplitude and kinetics do not change; and (4) the slow component of the EPSC in paired recordings increases with age and is highly temperature sensitive. Our data indicate that, although postsynaptic AMPARs in AII-AC dendrites are subject to desensitization (Figure 6), the sustained component of the light response and the evoked EPSCs in paired recordings both become larger with age after eye opening (Figures 1 and 3). Finally, our quantal deconvolution analysis indicates that the readily releasable pool of vesicles in RBCs also becomes larger during synaptic maturation.

The development of dual-component EPSCs after eye opening

Our findings indicate that synaptic strength increases in the mammalian retina after eye opening. In mouse primary visual cortex, neurons are already highly selective for visual stimuli at the time of eye opening, but extensive reorganization continues afterward.[5,73,74] Previous developmental studies have shown that the number of synaptic ribbons increases from P11 to P15 and further still at P21 in mouse ON bipolar cells.[75] These changes mirror the increase in the fast and slow EPSC charge from P14–P20 to P30–P44 in paired recordings (Figure 3D). Synaptic ribbon numbers in adult RBCs vary from 36 in rat retina[43] to 24–53 in mouse RBCs.[56,76,77] There are about 7–12 ribbon synapses between one RBC and one AII-AC in rat,[43] but in mouse retina EM estimates indicate as many as 24–35 ribbons from one RBC contact onto one AII-AC.[56] This large number may underpin the robust dual-component EPSC of the mature synapse.

Our results show that spontaneous mEPSC frequency greatly increases with age (Figures 4Bii and Cii), suggesting that vesicles become more fusion competent as the synapse matures. The amplitude distribution of mEPSCs was highly skewed to the left, because of the presence of large mEPSCs. In both the young and the mature groups, the distribution is well fit by a log-normal function (Figure 4Bi). In the presence of 10 mM L-AP4, the skewness parameter s for mature synapses decreased significantly from 1.58 to 1.35 (see Table S1), but the distribution was still better fit by a log-normal function than a symmetric Gaussian function. Additional application of 100 μM Cd^{2+} still left the distribution log normal (Figure S2), although mEPSC frequency was reduced. We thus suggest that single vesicles are released under 10 μM L-AP4. Interestingly, the single-quantum mEPSC amplitude distributions are Gaussian for P43 mossy fiber synapses, but they are highly skewed for immature P11 synapses.[78] Our results are thus broadly consistent with large-amplitude mEPSCs being due to coordinated multivesicular release due to stochastic openings of co-localized Ca^{2+} channels and docked vesicles.[14,43,79]

Our studies reveal two distinct release components during RBC synapse maturation. This phenomenon is more apparent at near PT, perhaps due to the increase in presynaptic Ca^{2+} currents (Figure 5A, top). Phasic and sustained exocytosis is also seen with C_m measurements in RBCs.[80,81] The vesicle pool size was significantly enhanced at higher

temperatures, suggesting an increase in collision frequency of vesicles with the ribbon structure[82] and/or more recruitment to non-ribbon release sites.[31] We found that both evoked EPSC amplitudes (Figure 3) and the readily releasable pool of vesicles are significantly increased in more mature synapses, suggesting that ribbon synapse maturation leads to an enhanced capacity for continuous exocytosis. This could be achieved in part by co-localization between Ca^{2+} channels and docked vesicles in mature synapses, given that we also observed that synaptic delay of evoked EPSCs becomes shorter in mature synapses (Figure 3D, inset).[34]

The mechanisms that generate the slow components of the dual-component EPSCs are not well understood. Full deletion of RIBEYE, the major ribbon-specific protein, severely reduced the fast and slow components of the EPSC.[83] However, non-ribbon-mediated exocytosis has also been reported in bipolar cell terminals.[28,29,31] In goldfish bipolar cell terminals, vesicle clusters have been observed at postsynaptic densities that are not ribbon associated.[28,84–86]

Light-evoked EPSCs at AII-ACs and their quantal content

AII-ACs make gap-junction connections with ON-type cone bipolar cells. Previous recordings from AII-ACs have indicated the presence of light-evoked currents arising from these gap-junction connections.[41,87] We considered the possibility that these gap junctions might underlie the sustained component of the EPSCs in our recordings. A hallmark of such electrical synapses is that the I-V relation is non-linear, since the inputs cannot be reversed under voltage clamp (see Figure 1).[41] It is worth noting that the background intensities used were higher, which will promote coupling.[38] In contrast, the I-V relations in our recordings were essentially linear, with a reversal potential close to 0 mV, as expected for AMPAR channels. Moreover, the I-V relations in Cx36-KO mice and wild-type mice were similar. These findings provide compelling evidence against their being a strong input through gap junctions (Figure 2). Previous work has demonstrated the presence of CP-AMPARs at the RBC-to-AII-AC synapse, which should display a non-linear (rectified) I-V relation.[27] Rectification is due to voltage-dependent block of the channels by endogenous spermines.[88] It thus seems likely that endogenous spermines were dialyzed out of the cells during the whole-cell recording, resulting in a relatively linear I-V relation. Another possibility is that rectification is “diluted” by activation of extrasynaptic Ca^{2+}-impermeable AMPARs that have linear I-V relations.[89] The finding that the EPSC amplitudes were smaller in the Cx36-KO mice compared to wild-type mice was unexpected (Figures 1A, 1C, and 2D). It is possible that homeostasis changes the synaptic gain within the circuit when Cx36 is globally knocked out.[90]

What are the physiological roles of the fast and slow components of exocytosis from RBC terminals (Figures 3 and 6) that give rise to the transient and sustained light-evoked EPSCs in AII-ACs (Figures 1 and 2)? Previous analyses proposed that the sustained component encoded luminance and the fast component contrast.[9,23] A key finding is that the threshold intensity for activation of the fast component of the light-evoked EPSCs in AII-ACs was about an order of magnitude higher than for the slow component, suggesting that the slow component may carry different information depending upon

luminance level. The rod pathway operates under two regimes. At visual threshold when photons are limiting, luminance is essentially zero, and RBCs pass single-photon signals to the AII-ACs. As ambient light intensity increases to middle to high scotopic levels, the continuous rain of photons generates a background luminance signal, and the RBCs signal both luminance and contrast. We propose that when single RBCs are detecting one or zero photons per integration time, the slow component of the transmitter release from RBCs carries the bulk of the visual signal. Indeed, in previous recordings of EPSCs from mouse AII-ACs at scotopic backgrounds a fast component was not evident; the responses appeared to be mediated entirely by the slow component.[87] Our finding that the time course of the slow EPSCs in AII-ACs matches the time course of single-photon events in mammalian photoreceptors[91,92] and bipolar cells[93,94] suggests that the synapse may effectively implement a matched filter that more faithfully transmits the single-photon signals. The relatively high threshold for activation of the fast, transient component of transmitter release from the RBCs is consistent with the notion that this component signals contrast at middle to high scotopic levels, while the slow component now carries a luminance signal, as has been proposed.[9,23] It is worth noting, however, that the previous paired recording experiments were performed at RT. Here, we show that evoked EPSCs have a strong temperature dependence. Therefore, the relative contributions to RBC signaling of the fast and slow components reflect *in vivo* conditions only at PTs.

We propose that the slower sustained component of the EPSCs would be able to generate reliable crossover glycinergic inhibition[95–99] onto OFF cone bipolar cells in photopic conditions[22,97] in addition to luminance signals to the retinal circuits. AII-ACs also form direct glycinergic synapses onto OFF ganglion cells.[100–102] Therefore, the strength of crossover inhibition onto OFF cone bipolar cells or direct OFF ganglion cells would be increased by stronger excitatory inputs to AII-AC dendrites after eye opening.

What is the quantal content of the light-evoked EPSC? The single-quantum mEPSC charge is 27 fC (Table S1; holding at −70 mV and at PT). The EPSC evoked by a 20 ms light flash lasts about a second, and the Q_{Fast} is 8 pC and Q_{Slow} is 100 pC (mature AII-AC; Figure 1). The Q_{Fast} is thus 296 quanta and Q_{Slow} is 3,703 quanta, so the total quantal content is ~4,000 vesicles. This may be an underestimate due to AMPAR desensitization. The 200 ms depolarizing pulse in paired recordings has a quantal content at PT of about 220 vesicles (Figure 6H). Given that the light response lasts 5-fold longer and involves three or four predominant RBC inputs onto a single AII-AC,[56] there appears to be a good agreement between our paired recordings and light-evoked EPSCs. By contrast, the quantal content of the OFF-light response in retinal ganglion cells is only 200 vesicles at RT in salamander.[103] Impressive amounts of vesicles are thus being released onto a single AII-AC with just a brief light flash.

Limitations of the study

In the presence of CTZ, mEPSC amplitudes increased, and their decay was substantially slower in the young age group (Figure 6B),[13] whereas we did not observe a change in mEPSC amplitude in the mature age group (Figure 6F).[51] Surprisingly, our results thus suggest that AMPAR desensitization may be more prominent in mature synapses that release

more glutamate than in young synapses. However, we note that CTZ not only blocks AMPAR desensitization, but it also increases receptor affinity.[61]

AMPAR saturation is another factor that limits EPSC amplitudes and, thus, estimates of vesicle pool size.[104] Previous studies have suggested, however, that there may be no AMPAR saturation during the sustained phase of release.[13,15,34] Imaging studies using genetically expressed fluorescent glutamate indicators may provide an alternative path toward further insights.[105]

STAR★METHODS

RESOURCE AVAILABILITY

Lead contact—Further information and requests for resources and reagents should be directed to and will be fulfilled by the Lead Contact: Mean-Hwan Kim (meanhwan@gmail.com).

Materials availability—No novel reagents were generated by this study.

Data and code availability

- Data reported in this paper will be shared by the lead contact upon request.
- Original codes to detect miniature EPSCs has been deposited at Github and is publicly available. Link is provided in the key resources table.
- Any additional information required to reanalyze the data reported in this paper is available from the lead contact upon request.

EXPERIMENTAL MODEL AND SUBJECT DETAILS

Animals—All the procedures were conducted in accordance with the guidelines approved by the Institutional Animal Care and Use Committee of Oregon Health & Science University. Mouse retinas were isolated from wild type mice (C57BL/6, Jackson Lab. or Charles River Lab.) and Cx36 knockout mice (generated using heterozygous crossing[106]) of either sex were housed in the OHSU Department of Comparative Medicine. The mice were deeply anaesthetized with isoflurane (Nova plus Pharmaceuticals) and decapitated before eye removal. Retinas were dissected free of the eyecup in carbogen-bubbled (95% O_2, 5% CO_2) Ames medium (US biologicals) at room temperature.

METHOD DETAILS

Light responses in AII-ACs—For recordings of light-evoked responses, vertical slices of mouse retina (~300 μm) were prepared using a custom-made tissue slicer. Animals were dark-adapted for 1–2 hours. Anesthetization and all subsequent procedures were performed under infrared illumination to preserve the adaptation state. During recordings, cells were visualized and targeted under infrared illumination; however, the preparation was periodically exposed to dim red illumination from an LED (620 nm peak emission) when electrodes were replaced. Slices were transferred to the recording chamber and perfused at a rate of ~2 ml/min with bicarbonate-buffered Ames medium (US Biologicals) continuously

bubbled with 95% O_2, 5% CO_2. Slices were viewed with an Olympus BX51 upright microscope fitted with a 40x/0.8 water immersion objective and infrared gradient contrast optics. AII-ACs were identified by their characteristic morphology and light responses. Light response recordings were performed at 32–33°C.

Patch electrodes were fabricated from thick-walled borosilicate glass to have a resistance of 10–15 MΩ. The intracellular solution contained (in mM): K-methanesulfonate, 135; KCl, 6; Na2-ATP, 2; Na-GTP, 1; EGTA, 1; $MgCl_2$, 2; Na-HEPES, 5; and adjusted to pH 7.35 with KOH. Alexa 488 or 594 hydrazide (50–100 μM) was added to these solutions for morphological identification of recorded cells. Whole-cell voltage-clamp recordings were made with a HEKA EPC-10 patch-clamp amplifier. To minimize possible contamination of the light-evoked currents with GABAergic or glycinergic currents,[107] we set the holding potential to −70 mV, close to the predicted chloride equilibrium potential. Light responses were elicited by diffuse illumination at a peak wavelength of 525 nm, using a LED projected through the microscope eyepiece and focused onto the preparation. Flash intensities were varied by altering the duration of the flash from 0.01 to 20 ms, which are within the integration time of mouse rod photoreceptors (~200 ms).[91] Light intensity was calculated using a UDT photometer (UDT Instruments, San Diego, CA, USA) and converted to photons/μm^2.

Paired recordings between RBC and AII-AC—Slices (200–250 μm) were made from retina embedded in low melting temperature agarose (sigma type VIIA, 3% in Ames medium).[108] Retinal slice was visualized using infrared-differential interference contrast (DIC) microscopy and a 60x water-immersion objective (Olympus). Whole-cell voltage-clamp recordings were obtained using 7–12 MΩ pulled from thick-walled borosilicate glass (1B150F-4; World Precision Instruments) using vertical puller (Narishige, PP-830) and performed at room temperature (RT, ~24°C) or near physiological temperature (PT, ~34°C) in mesopic conditions. For fine control of bath temperature, the temperature feedback sensor was attached on the bottom of objective and continuously monitored during experiments. Alexa 488 hydrazide for AII-AC and Alexa 594 hydrazide for RBC (50–100 μM) were added to the pipette solution for morphological identification of recorded cells. Whole-cell voltage-clamp recordings were made with a HEKA EPC-9 double patch-clamp amplifier.

The intracellular solution for both RBC and AII-AC contained (in mM): CsCl, 50; Cs-gluconate, 50; TEA-Cl 10; HEPES, 28; ATP-Mg, 3; GTP-Na, 1; EGTA, 2; Phospho-creatine, 10; pH 7.2 adjusted with CsOH. External bicarbonate-buffered Ames medium (US Biologicals) continuously bubbled with 95% O_2, 5% CO_2 was perfused. To reduce standing holding currents in mesopic condition, 10 μM L-AP4 was applied all the paired and mEPSC recordings.[43] In addition, 100 μM picrotoxin, 50 μM TPMPA, 0.5 μM strychnine, 0.25 μM TTX was included in Ames medium to block $GABA_A$, $GABA_C$, glycine receptor currents and voltage-gated Na^+ channel currents, respectively. Pipette series resistances (R_s) was 28.8 ± 10.2 MΩ in RBCs (mean ± s.d.; n = 12 cells) and Rs = 23.4 ± 4.1 MΩ in AII-ACs (mean ± s.d.; n = 10 cells) in paired voltage-clamp recordings.

For spontaneous mEPSCs recordings from AII-ACs, we used the same internal solution for paired recording described above or we used (in mM): Cs-gluconate, 126; HEPES, 10;

TEA-Cl, 5; Phospho-creatine, 5; ATP-Mg, 4; EGTA, 5; GTP-Na, 0.5; QX-314 Chloride, 4; pH 7.2 adjusted with CsOH. For the latter case 50 μM *D,L*-AP5 was also included in the external Ames medium, in addition to all the other blockers described above (i.e., 100 μM picrotoxin, 50 μM TPMPA, 0.5 μM strychnine, 0.25 μM TTX). This reduced the standing holding currents in mesopic condition in the AII-AC due perhaps to extrasynaptic NMDA receptors.[51,52] Reported holding potentials were corrected for the liquid junction potential, which was calculated to be ~10 mV unless otherwise noted. Alexa 488 and 594 hydrazide fluorescent dyes were purchased from Invitrogen. Average pipette series resistance was 13.1 ± 2 MΩ in AII-ACs (mean ± s.d.; n = 33 cells) in mEPSCs voltage-clamp recordings.

Deconvolution of evoked EPSCs—Calculation of the instantaneous release rate was carried out using custom algorithms in Igor Pro (Figures 5, 6, and S4; Wavemetrics). For this calculation, it was assumed that the EPSC signal, $s(t)$, is equal to the instantaneous release rate, $r_i(t)$, convolved with the quantal (single vesicle) event, $q(t)$, plus a continuous noise term, $n(t)$:

$$\mathbf{s}(t) = q(t) \cdot r_i(t) + n(t)$$

(Equation 1)

Here, $q(t)$ was determined for each cell and experimental condition as the average of several spontaneous mEPSCs detected by matched-filter analysis. Linear convolution is assumed, i.e., postsynaptic receptors are not desensitized or saturated during depolarization.[27]

The Fourier transform of the continuous release rate ($R_c(f)$) was then approximated using the Wiener deconvolution method,

$$R_c(f) \approx \frac{S(f)}{Q(f)} \frac{|Q(f)|^2}{|Q(f)|^2 + \frac{1}{\Phi(f)}}$$

(Equation 2)

where $S(f)$ and $Q(f)$ are the Fourier transforms of $s(t)$ and $q(t)$, respectively, and $\Phi(f)$ is the signal-to-noise power spectrum ratio. The power spectrum of the noise was determined from a baseline current recorded while the presynaptic cell was hyperpolarized. It was assumed that the noise statistics did not change during an evoked response. The power spectrum of the signal was justifiably assumed to be equal to that of the relatively low-noise estimation of $q(t)$.

The continuous release rate was given by the inverse Fourier transform of $R_c(f)$. We then calculated $r_i(t)$ from the continuous release rate by applying a modest threshold and integrating around the remaining inflection points. Integration intervals were taken as the midpoints between successive inflection points. Acceptable threshold values were determined by comparing the reconvolution ($r_i(t)*q(t)$) with the original EPSC, a process which also served to validate this method (see Figure S4).

Data analysis and statistics—mEPSCs detection (combined template and threshold routine) and analysis was done in IGOR Pro 8 and in Python (SciPy and NumPy libraries), using custom routines. It is based on a "sliding template method" with a detection threshold that is set above the baseline noise by 1 or 2 standard deviations.[109,110] Statistical tests were done in GraphPad Prism 9. The two-tailed, pairwise, non-pairwise t-test, and two-way ANOVA were used to determine statistical significance. A value of $p < 0.05$ was considered significant. In figures asterisks denote statistical significance (*; $p < 0.05$). Reported values are mean ± standard deviation or standard error of mean (SEM). Off-line analysis of the data was performed with Igor Pro software (Wavemetrics), MATLAB (MathWorks), and Excel (Microsoft).

Supplementary Material

Refer to Web version on PubMed Central for supplementary material.

ACKNOWLEDGMENTS

We thank all the members of the H.v.G. and W.R.T labs for extensive scientific discussions and Chad Grabner for insightful discussions on ribbon synapses. This work is funded by NIH grants EY014043, DC012938, EY032564 (H.v.G.), EY032965 (W.R.T.), and EY024265 (T.P).

REFERENCES

1. Matthews G, and Fuchs P (2010). The diverse roles of ribbon synapses in sensory neurotransmission. Nat. Rev. Neurosci. 11, 812–822. [PubMed: 21045860]
2. Schnee ME, Santos-Sacchi J, Castellano-Muñoz M, Kong JH, and Ricci AJ (2011). Calcium-dependent synaptic vesicle trafficking underlies indefatigable release at the hair cell afferent fiber synapse. Neuron 70, 326–338. [PubMed: 21521617]
3. Kim MH, Li GL, and von Gersdorff H (2013). Single Ca^{2+} channels and exocytosis at sensory synapses. J. Physiol. 591, 3167–3178. [PubMed: 23459757]
4. Lagnado L, and Schmitz F (2015). Ribbon synapses and visual processing in the retina. Annu. Rev. Vis. Sci. 1, 235–262. [PubMed: 28532378]
5. Ichinose T, and Habib S (2022). On and off signaling pathways in the retina and the visual system. Front. Ophthalmol. 2, 989002.
6. von Gersdorff H, Sakaba T, Berglund K, and Tachibana M (1998). Submillisecond kinetics of glutamate release from a sensory synapse. Neuron 21, 1177–1188. [PubMed: 9856472]
7. Grabner CP, and Zenisek D (2013). Amperometric resolution of a pre-spike stammer and evoked phases of fast release from retinal bipolar cells. J. Neurosci. 33, 8144–8158. [PubMed: 23658155]
8. Babai N, Bartoletti TM, and Thoreson WB (2010). Calcium regulates vesicle replenishment at the cone ribbon synapse. J. Neurosci. 30, 15866–15877. [PubMed: 21106825]
9. Oesch NW, and Diamond JS (2011). Ribbon synapses compute temporal contrast and encode luminance in retinal rod bipolar cells. Nat. Neurosci. 14, 1555–1561. [PubMed: 22019730]
10. Davison A, Gierke K, Brandstätter JH, and Babai N (2022). Functional and structural development of mouse cone photoreceptor ribbon synapses. Invest. Ophthalmol. Vis. Sci. 63, 21.
11. Wachtmeister L (1998). Oscillatory potentials in the retina: what do they reveal. Prog. Retin. Eye Res. 17, 485–521. [PubMed: 9777648]
12. He Q, Xu HP, Wang P, and Tian N (2013). Dopamine D1 receptors regulate the light dependent development of retinal synaptic responses. PLoS One 8, e79625. [PubMed: 24260267]
13. Singer JH, and Diamond JS (2006). Vesicle depletion and synaptic depression at a mammalian ribbon synapse. J. Neurophysiol. 95, 3191–3198. [PubMed: 16452253]

14. Mehta B, Snellman J, Chen S, Li W, and Zenisek D (2013). Synaptic ribbons influence the size and frequency of miniature-like evoked postsynaptic currents. Neuron 77, 516–527. [PubMed: 23395377]
15. Kim MH, and von Gersdorff H (2016). Postsynaptic plasticity triggered by Ca^{2+}-permeable AMPA receptor activation in retinal amacrine cells. Neuron 89, 507–520. [PubMed: 26804991]
16. Wark B, Fairhall A, and Rieke F (2009). Timescales of inference in visual adaptation. Neuron 61, 750–761. [PubMed: 19285471]
17. Snellman J, Zenisek D, and Nawy S (2009). Switching between transient and sustained signalling at the rod bipolar-AII amacrine cell synapse of the mouse retina. J. Physiol. 587, 2443–2455. [PubMed: 19332496]
18. Palmer MJ (2010). Characterisation of bipolar cell synaptic transmission in goldfish retina using paired recordings. J. Physiol. 588, 1489–1498. [PubMed: 20211975]
19. Puthussery T, Gayet-Primo J, and Taylor WR (2011). Carbonic anhydrase-related protein VIII is expressed in rod bipolar cells and alters signaling at the rod bipolar to AII-amacrine cell synapse in the mammalian retina. Eur. J. Neurosci. 34, 1419–1431. [PubMed: 22004450]
20. Wei HP, Yao YY, Zhang RW, Zhao XF, and Du J.l. (2012). Activity-induced long-term potentiation of excitatory synapses in developing zebrafish retina in vivo. Neuron 75, 479–489. [PubMed: 22884331]
21. Ke JB, Wang YV, Borghuis BG, Cembrowski MS, Riecke H, Kath WL, Demb JB, and Singer JH (2014). Adaptation to background light enables contrast coding at rod bipolar cell synapses. Neuron 81, 388–401. [PubMed: 24373883]
22. Graydon CW, Lieberman EE, Rho N, Briggman KL, Singer JH, and Diamond JS (2018). Synaptic transfer between rod and cone pathways mediated by AII amacrine cells in the mouse retina. Curr. Biol. 28, 2739–2751.e3. [PubMed: 30122532]
23. Jarsky T, Cembrowski M, Logan SM, Kath WL, Riecke H, Demb JB, and Singer JH (2011). A synaptic mechanism for retinal adaptation to luminance and contrast. J. Neurosci. 31, 11003–11015. [PubMed: 21795549]
24. Zenisek D, Steyer JA, and Almers W (2000). Transport, capture and exocytosis of single synaptic vesicles at active zones. Nature 406, 849–854. [PubMed: 10972279]
25. Snellman J, Mehta B, Babai N, Bartoletti TM, Akmentin W, Francis A, Matthews G, Thoreson W, and Zenisek D (2011). Acute destruction of the synaptic ribbon reveals a role for the ribbon in vesicle priming. Nat. Neurosci. 14, 1135–1141. [PubMed: 21785435]
26. Mørkve SH, Veruki ML, and Hartveit E (2002). Functional characteristics of non-NMDA-type ionotropic glutamate receptor channels in AII amacrine cells in rat retina. J. Physiol. 542, 147–165. [PubMed: 12096058]
27. Singer JH, and Diamond JS (2003). Sustained Ca^{2+} entry elicits transient postsynaptic currents at a retinal ribbon synapse. J. Neurosci. 23, 10923–10933. [PubMed: 14645488]
28. Midorikawa M, Tsukamoto Y, Berglund K, Ishii M, and Tachibana M (2007). Different roles of ribbon-associated and ribbon-free active zones in retinal bipolar cells. Nat. Neurosci. 10, 1268–1276. [PubMed: 17828257]
29. Zenisek D (2008). Vesicle association and exocytosis at ribbon and extraribbon sites in retinal bipolar cell presynaptic terminals. Proc. Natl. Acad. Sci. USA 105, 4922–4927. [PubMed: 18339810]
30. Chen M, Van Hook MJ, Zenisek D, and Thoreson WB (2013). Properties of ribbon and non-ribbon release from rod photoreceptors revealed by visualizing individual synaptic vesicles. J. Neurosci. 33, 2071–2086. [PubMed: 23365244]
31. Mehta B, Ke JB, Zhang L, Baden AD, Markowitz AL, Nayak S, Briggman KL, Zenisek D, and Singer JH (2014). Global Ca^{2+} signaling drives ribbon-independent synaptic transmission at rod bipolar cell synapses. J. Neurosci. 34, 6233–6244. [PubMed: 24790194]
32. Cadetti L, Tranchina D, and Thoreson WB (2005). A comparison of release kinetics and glutamate receptor properties in shaping rod-cone differences in EPSC kinetics in the salamander retina. J. Physiol. 569, 773–788. [PubMed: 16223761]
33. Tian M, Xu CS, Montpetit R, and Kramer RH (2012). Rab3A mediates vesicle delivery at photoreceptor ribbon synapses. J. Neurosci. 32, 6931–6936. [PubMed: 22593061]

34. Jarsky T, Tian M, and Singer JH (2010). Nanodomain control of exocytosis is responsible for the signaling capability of a retinal ribbon synapse. J. Neurosci. 30, 11885–11895. [PubMed: 20826653]
35. Hartveit E, Veruki ML, and Zandt BJ (2022). Dendritic morphology of an inhibitory retinal interneuron enables simultaneous local and global synaptic integration. J. Neurosci. 42, 1630–1647. [PubMed: 35017223]
36. Hampson EC, Vaney DI, and Weiler R (1992). Dopaminergic modulation of gap junction permeability between amacrine cells in mammalian retina. J. Neurosci. 12, 4911–4922. [PubMed: 1281499]
37. Baldridge WH, Vaney DI, and Weiler R (1998). The modulation of intercellular coupling in the retina. Semin. Cell Dev. Biol. 9, 311–318. [PubMed: 9665867]
38. Bloomfield SA, and Völgyi B (2004). Function and plasticity of homologous coupling between AII amacrine cells. Vision Res. 44, 3297–3306. [PubMed: 15535997]
39. Kothmann WW, Massey SC, and O'Brien J (2009). Dopamine-stimulated dephosphorylation of connexin 36 mediates AII amacrine cell uncoupling. J. Neurosci. 29, 14903–14911. [PubMed: 19940186]
40. Trexler EB, Li W, and Massey SC (2005). Simultaneous contribution of two rod pathways to AII amacrine and cone bipolar cell light responses. J. Neurophysiol. 93, 1476–1485. [PubMed: 15525810]
41. Pang JJ, Abd-El-Barr MM, Gao F, Bramblett DE, Paul DL, and Wu SM (2007). Relative contributions of rod and cone bipolar cell inputs to AII amacrine cell light responses in the mouse retina. J. Physiol. 580, 397–410. [PubMed: 17255172]
42. Berntson A, Smith RG, and Taylor WR (2004). Postsynaptic calcium feedback between rods and rod bipolar cells in the mouse retina. Vis. Neurosci. 21, 913–924. [PubMed: 15733346]
43. Singer JH, Lassová L, Vardi N, and Diamond JS (2004). Coordinated multivesicular release at a mammalian ribbon synapse. Nat. Neurosci. 7, 826–833. [PubMed: 15235608]
44. Taylor WR (1988). Permeation of barium and cadmium through slowly inactivating calcium channels in cat sensory neurones. J. Physiol. 407, 433–452. [PubMed: 2855742]
45. Tsintsadze T, Williams CL, Weingarten DJ, von Gersdorff H, and Smith SM (2017). Distinct actions of voltage-activated Ca^{2+} channel block on spontaneous release at excitatory and inhibitory central synapses. J. Neurosci. 37, 4301–4310. [PubMed: 28320843]
46. Chávez AE, Singer JH, and Diamond JS (2006). Fast neurotransmitter release triggered by Ca influx through AMPA-type glutamate receptors. Nature 443, 705–708. [PubMed: 17036006]
47. Osswald IK, Galan A, and Bowie D (2007). Light triggers expression of philanthotoxin-insensitive Ca^{2+}-permeable AMPA receptors in the developing rat retina. J. Physiol. 582, 95–111. [PubMed: 17430992]
48. Schlesinger F, Tammena D, Krampfl K, and Bufler J (2005). Two mechanisms of action of the adamantane derivative IEM-1460 at human AMPA-type glutamate receptors. Br. J. Pharmacol. 145, 656–663. [PubMed: 15834439]
49. Fortin DA, Davare MA, Srivastava T, Brady JD, Nygaard S, Derkach VA, and Soderling TR (2010). Long-term potentiation-dependent spine enlargement requires synaptic Ca^{2+}-permeable AMPA receptors recruited by CaM-kinase I. J. Neurosci. 30, 11565–11575. [PubMed: 20810878]
50. Percival KA, Gayet J, Khanjian R, Taylor WR, and Puthussery T (2022). Calcium-permeable AMPA receptors on AII amacrine cells mediate sustained signaling in the On-pathway of the primate retina. Cell Rep. 41, 111484. [PubMed: 36223749]
51. Veruki ML, Mørkve SH, and Hartveit E (2003). Functional properties of spontaneous EPSCs and non-NMDA receptors in rod amacrine (AII) cells in the rat retina. J. Physiol. 549, 759–774. [PubMed: 12702738]
52. Zhou Y, Tencerová B, Hartveit E, and Veruki ML (2016). Functional NMDA receptors are expressed by both AII and A17 amacrine cells in the rod pathway of the mammalian retina. J. Neurophysiol. 115, 389–403. [PubMed: 26561610]
53. Kushmerick C, Renden R, and von Gersdorff H (2006). Physiological temperatures reduce the rate of vesicle pool depletion and short-term depression via an acceleration of vesicle recruitment. J. Neurosci. 26, 1366–1377. [PubMed: 16452660]

54. van Hook MJ (2020). Temperature effects on synaptic transmission and neuronal function in the visual thalamus. PLoS One 15, e0232451. [PubMed: 32353050]
55. Dunn FA, and Wong ROL (2012). Diverse strategies engaged in establishing stereotypic wiring patterns among neurons sharing a common input at the visual system's first synapse. J. Neurosci. 32, 10306–10317. [PubMed: 22836264]
56. Tsukamoto Y, and Omi N (2013). Functional allocation of synaptic contacts in microcircuits from rods via rod bipolar to AII amacrine cells in the mouse retina. J. Comp. Neurol. 521, 3541–3555. [PubMed: 23749582]
57. Sagdullaev BT, McCall MA, and Lukasiewicz PD (2006). Presynaptic inhibition modulates spillover, creating distinct dynamic response ranges of sensory output. Neuron 50, 923–935. [PubMed: 16772173]
58. Grabner CP, Ratliff CP, Light AC, and DeVries SH (2016). Mechanism of high-frequency signaling at a depressing ribbon synapse. Neuron 91, 133–145. [PubMed: 27292536]
59. Patneau DK, Vyklicky L Jr., and Mayer ML (1993). Hippocampal neurons exhibit cyclothiazide-sensitive rapidly desensitizing responses to kainite. J. Neurosci. 13, 3496–3509. [PubMed: 7688040]
60. Yamada KA, and Tang CM (1993). Benzothiadiazides inhibit rapid glutamate receptor desensitization and enhance glutamatergic synaptic currents. J. Neurosci. 13, 3904–3915. [PubMed: 8103555]
61. Diamond JS, and Jahr CE (1995). Asynchronous release of synaptic vesicles determines the time course of the AMPA receptor-mediated EPSC. Neuron 15, 1097–1107. [PubMed: 7576653]
62. Rodriguez-Contreras A, and Yamoah EN (2001). Direct measurement of single-channel Ca^{2+} currents in bullfrog hair cells reveals two distinct channel subtypes. J. Physiol. 534, 669–689. [PubMed: 11483699]
63. Zampini V, Johnson SL, Franz C, Lawrence ND, Münkner S, Engel J, Knipper M, Magistretti J, Masetto S, and Marcotti W (2010). Elementary properties of Cav1.3 Ca^{2+} channels expressed in mouse cochlear inner cells. J. Physiol. 588, 187–199. [PubMed: 19917569]
64. Bartoletti TM, Jackman SL, Babai N, Mercer AJ, Kramer RH, and Thoreson WB (2011). Release from the cone ribbon synapse under bright light conditions can be controlled by the opening of only a few Ca^{2+} channels. J. Neurophysiol. 106, 2922–2935. [PubMed: 21880934]
65. Veruki ML, Mørkve SH, and Hartveit E (2006). Activation of a presynaptic glutamate transporter regulates synaptic transmission through electrical signaling. Nat. Neurosci. 9, 1388–1396. [PubMed: 17041592]
66. Wersinger E, Schwab Y, Sahel JA, Rendon A, Pow DV, Picaud S, and Roux MJ (2006). The glutamate transporter EAAT5 works as a presynaptic receptor in mouse rod bipolar cells. J. Physiol. 577, 221–234. [PubMed: 16973698]
67. Gehlen J, Aretzweiler C, Mataruga A, Fahlke C, and Müller F (2021). Excitatory amino acid transporter EAAT5 improves temporal resolution in the retina. eNeuro 8. ENEURO.0406–21.2021.
68. Palmer MJ, Taschenberger H, Hull C, Tremere L, and von Gersdorff H (2003). Synaptic activation of presynaptic glutamate transporter currents in nerve terminals. J. Neurosci. 23, 4831–4841. [PubMed: 12832505]
69. Rossi DJ, Alford S, Mugnaini E, and Slater NT (1995). Properties of transmission at a giant glutamatergic synapse in cerebellum: the mossy fiber-unipolar brush cell synapse. J. Neurophysiol. 74, 24–42. [PubMed: 7472327]
70. DeVries SH (2001). Exocytosed protons feedback to suppress the Ca^{2+} current in mammalian cone photoreceptors. Neuron 32, 1107–1117. [PubMed: 11754841]
71. Palmer MJ, Hull C, Vigh J, and von Gersdorff H (2003). Synaptic cleft acidification and modulation of short-term depression by exocytosed protons in retinal bipolar cells. J. Neurosci. 23, 11332–11341. [PubMed: 14672997]
72. Tang FS, Yuan HL, Liu JB, Zhang G, Chen SY, and Ke JB (2022). Glutamate transporters EAAT2 and EAAT5 differentially shape synaptic transmission from rod bipolar cell terminals. eNeuro 9. ENEURO.0074.
73. Ko H, Cossell L, Baragli C, Antolik J, Clopath C, Hofer SB, and Mrsic-Flogel TD (2013). The emergence of functional microcircuits in visual cortex. Nature 496, 96–100. [PubMed: 23552948]

74. Kerschensteiner D (2022). Feature detection by retinal ganglion cells. Annu. Rev. Vis. Sci. 8, 135–169. [PubMed: 35385673]
75. Okawa H, Yu W-Q, Matti U, Schwarz K, Odermatt B, Zhong H, Tsukamoto Y, Lagnado L, Rieke F, Schmitz F, and Wong ROL (2019). Dynamic assembly of ribbon synapses and circuit maintenance in a vertebrate sensory system. Nat. Commun. 10, 2167. [PubMed: 31092821]
76. LoGiudice L, Sterling P, and Matthews G (2009). Vesicle recycling at ribbon synapses in the finely branched axon terminals of mouse retinal bipolar neurons. Neuroscience 164, 1546–1556. [PubMed: 19778591]
77. Wan QF, and Heidelberger R (2011). Synaptic release at mammalian bipolar cell terminals. Vis. Neurosci. 28, 109–119. [PubMed: 21272392]
78. Wall MJ, and Usowicz MM (1998). Development of the quantal properties of evoked and spontaneous synaptic currents at a brain synapse. Nat. Neurosci. 1, 675–682. [PubMed: 10196583]
79. Wong AB, Rutherford MA, Gabrielaitis M, Pangrsic T, Göttfert F, Frank T, Michanski S, Hell S, Wolf F, Wichmann C, and Moser T (2014). Developmental refinement of the hair cell synapses tightens the coupling of Ca^{2+} influx to exocytosis. EMBO J. 33, 247–264. [PubMed: 24442635]
80. Zhou ZY, Wan QF, Thakur P, and Heidelberger R (2006). Capacitance measurements in the mouse rod bipolar cell identify a pool of releasable synaptic vesicles. J. Neurophysiol. 96, 2539–2548. [PubMed: 16914610]
81. Oltedal L, and Hartveit E (2010). Transient release kinetics of rod bipolar cells revealed by capacitance measurement of exocytosis from axon terminals in rat retinal slices. J. Physiol. 588, 1469–1487. [PubMed: 20211976]
82. Graydon CW, Zhang J, Oesch NW, Sousa AA, Leapman RD, and Diamond JS (2014). Passive diffusion as a mechanism underlying ribbon synapse vesicle release and resupply. J. Neurosci. 34, 8948–8962. [PubMed: 24990916]
83. Maxeiner S, Luo F, Tan A, Schmitz F, and Südhof TC (2016). How to make a synaptic ribbon: RIBEYE deletion abolishes ribbons in retinal synapses and disrupts neurotransmitter release. EMBO J. 35, 1098–1114. [PubMed: 26929012]
84. Zenisek D, Davila V, Wan L, and Almers W (2003). Imaging calcium entry sites and ribbon structures in two presynaptic cells. J. Neurosci. 23, 2538–2548. [PubMed: 12684438]
85. Hull C, Studholme K, Yazulla S, and von Gersdorff H (2006). Diurnal changes in exocytosis and the number of synaptic ribbons at active zones of an ON-type bipolar cell terminal. J. Neurophysiol. 96, 2025–2033. [PubMed: 16738212]
86. Minami N, Berglund K, Sakaba T, Kohmoto H, and Tachibana M (1998). Potentiation of transmitter release by protein kinase C in goldfish retinal bipolar cells. J. Physiol. 512, 219–225. [PubMed: 9729631]
87. Murphy GJ, and Rieke F (2008). Signals and noise in an inhibitory interneuron diverge to control activity in nearby retinal ganglion cells. Nat. Neurosci. 11, 318–326. [PubMed: 18223648]
88. Koh DS, Burnashev N, and Jonas P (1995). Block of native Ca^{2+}-permeable AMPA receptors in rat brain by intracellular polyamines generates double rectification. J. Physiol. 486, 305–312. [PubMed: 7473198]
89. Jones RS, Pedisich M, Carroll RC, and Nawy S (2014). Spatial organization of AMPA subtypes in ON RGCs. J. Neurosci. 34, 656–661. [PubMed: 24403163]
90. Lazarevic V, Pothula S, Andres-Alonso M, and Fejtova A (2013). Molecular mechanisms driving homeostatic plasticity of neurotransmitter release. Front. Cell. Neurosci. 7, 244. [PubMed: 24348337]
91. Burns ME, Mendez A, Chen J, and Baylor DA (2002). Dynamics of cyclic GMP synthesis in retinal rods. Neuron 36, 81–91. [PubMed: 12367508]
92. Beier C, Bocchero U, Levy L, Zhang Z, Jin N, Massey SC, Ribelayga CP, Martemyanov K, Hattar S, and Pahlberg J (2022). Divergent outer retinal circuits drive image and non-image visual behaviors. Cell Rep. 39, 111003. [PubMed: 35767957]
93. Field GD, and Rieke F (2002). Nonlinear signal transfer from mouse rods to bipolar cells and implications for visual sensitivity. Neuron 34, 773–785. [PubMed: 12062023]
94. Berntson A, Smith RG, and Taylor WR (2004). Transmission of single photon signals through a binary synapse in the mammalian retina. Vis. Neurosci. 21, 693–702. [PubMed: 15683557]

95. Liang Z, and Freed MA (2010). The ON pathway rectifies the OFF pathway of the mammalian retina. J. Neurosci. 30, 5533–5543. [PubMed: 20410107]

96. Werblin FS (2010). Six different roles for crossover inhibition in the retina: Correcting the nonlinearities of synaptic transmission. Vis. Neurosci. 27, 1–8. [PubMed: 20392301]

97. Demb JB, and Singer JH (2012). Intrinsic properties and functional circuitry of the AII amacrine cell. Vis. Neurosci. 29, 51–60. [PubMed: 22310372]

98. Akrouh A, and Kerschensteiner D (2013). Intersecting circuits generate precisely patterned retinal waves. Neuron 79, 322–334. [PubMed: 23830830]

99. Rosa JM, Ruehle S, Ding H, and Lagnado L (2016). Crossover inhibition generates sustained visual responses in the inner retina. Neuron 90, 308–319. [PubMed: 27068790]

100. Manookin MB, Beaudoin DL, Ernst ZR, Flagel LJ, and Demb JB (2008). Disinhibition combines with excitation to extend the operating range of the OFF visual pathway in daylight. J. Neurosci. 28, 4136–4150. [PubMed: 18417693]

101. van Wyk M, Wässle H, and Taylor WR (2009). Receptive field properties of ON- and OFF-ganglion cells in the mouse retina. Vis. Neurosci. 26, 297–308. [PubMed: 19602302]

102. Arman AC, and Sampath AP (2012). Dark-adapted response threshold of OFF ganglion cells is not set by OFF bipolar cells in the mouse retina. J. Neurophysiol. 107, 2649–2659. [PubMed: 22338022]

103. Taylor WR, Chen E, and Copenhagen DR (1995). Characterization of spontaneous excitatory synaptic currents in salamander retinal ganglion cells. J. Physiol. 486, 207–221. [PubMed: 7562636]

104. Neher E, and Sakaba T (2001). Combining deconvolution and noise analysis for the estimation of transmitter release rates at the calyx of held. J. Neurosci. 21, 444–461. [PubMed: 11160425]

105. Armbruster M, Dulla CG, and Diamond JS (2020). Effects of fluorescent glutamate indicators on neurotransmitter diffusion and uptake. Elife 9, e54441. [PubMed: 32352378]

106. Hormuzdi SG, Pais I, LeBeau FE, Towers SK, Rozov A, Buhl EH, Whittington MA, and Monyer H (2001). Impaired electrical signaling disrupts gamma frequency oscillations in connexin 36-deficient mice. Neuron 31, 487–495. [PubMed: 11516404]

107. Vigh J, Vickers E, and von Gersdorff H (2011). Light-evoked lateral GABAergic inhibition at single bipolar cell synaptic terminals in driven by distinct retinal microcircuits. J. Neurosci. 31, 15884–15893. [PubMed: 22049431]

108. Kim MH, Vickers E, and von Gersdorff H (2012). Patch-clamp capacitance measurements and Ca^{2+} imaging at single nerve terminals in retinal slices. J. Vis. Exp. 59, 3345.

109. Jonas P, Major G, and Sakmann B (1993). Quantal components of unitary EPSCs at the mossy fibre synapse on CA3 pyramidal cells of rat hippocampus. J. Physiol. 472, 615–663. [PubMed: 7908327]

110. Clements JD, and Bekkers JM (1997). Detection of spontaneous synaptic events with an optimally scaled template. Biophys. J. 73, 220–229. [PubMed: 9199786]

Highlights

- The fast component of the light-evoked EPSC has a higher threshold than the slow component
- Spontaneous mEPSC frequency increases with age, but amplitude and kinetics do not change
- The EPSC charge in paired recordings increases with age and is highly temperature sensitive
- Synaptic vesicle pool size and AMPA receptor desensitization both increase with age

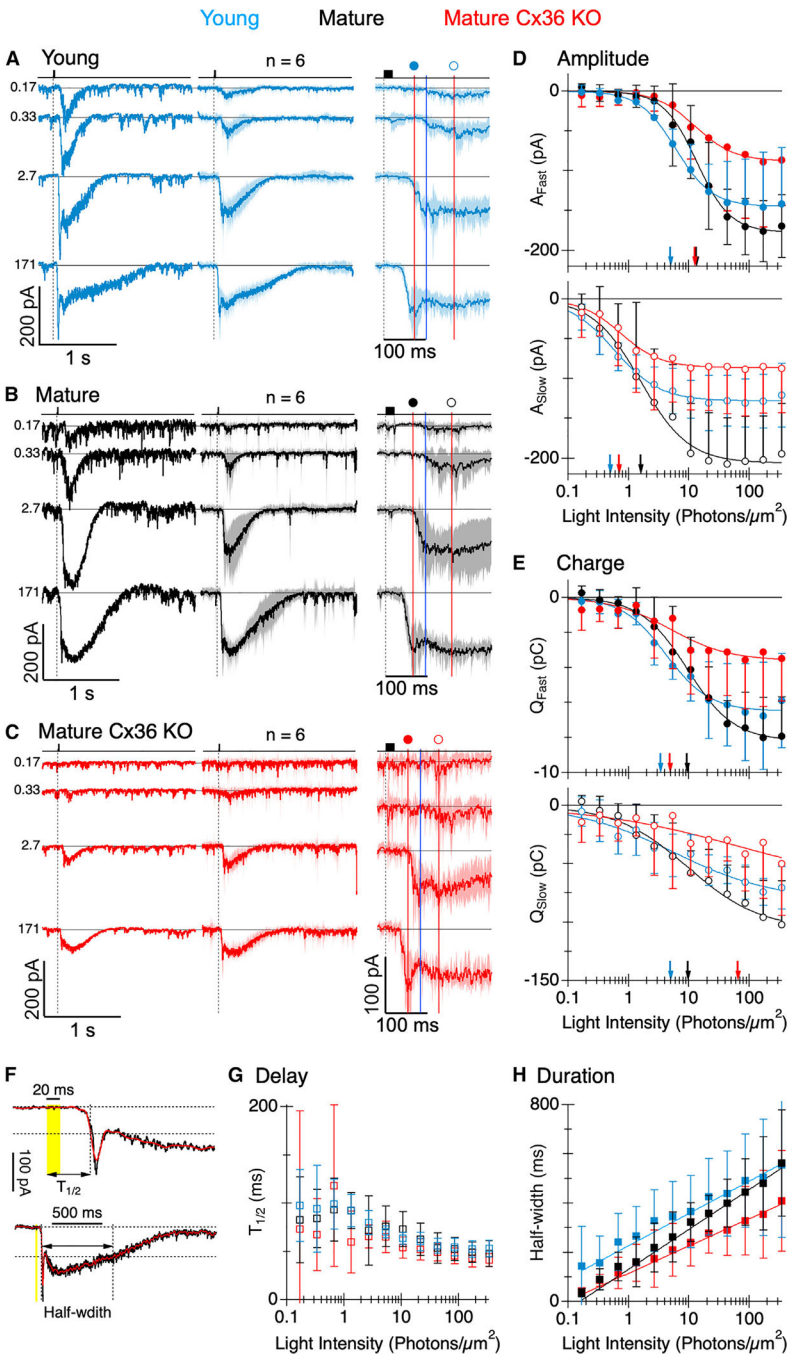

Figure 1. Flash responses in mouse AII-ACs display fast and slow components

(A–C) EPSCs evoked by light flashes in young (P16), mature (P38), and mature Cx36-KO mice (P38). The left traces show EPSCs in a representative cell, and the middle traces show average EPSCs from several cells (n = number of cells). Shading shows standard deviation. Stimulus timing is shown at the top. The numbers to the left of the traces show the flash intensities in photons/μm^2. The traces on the right show the average EPSCs on an expanded time base to better illustrate the two components. Red vertical lines show the measurement time points for the data points (with the corresponding symbols) in (D). The blue vertical

lines delineate “fast” and “slow” charge shown in (E). Fast charge is the integral from 0.2 s to the blue line. Slow charge is the integral from the blue line to 1.6 s.

(D) Amplitudes of the EPSCs at the two fixed time points shown in (A)–(C).

(E) Charge movement during the EPSCs over the intervals illustrated in (A)–(C). The smooth curves in (D) and (E) show fits to the Hill equation (see method details in the STAR Methods), with the half-max intensities indicated by the arrows on the x axes.

(F) Illustration of the measurement of the time-to-half-max ($T_{1/2}$) and the EPSC width at half-max (half-width). Measurements were performed on a filtered version of the trace (red overlays) to obviate early threshold crossing due to current variance.

(G) $T_{1/2}$ as a function of stimulus intensity for the three groups.

(H) Half-width as a function of stimulus intensity for the three groups. Solid lines show log-linear regression and indicate that the half-width increased exponentially as a function of stimulus strength. A two-way ANOVA (alpha = 0.05) revealed that the EPSCs in young retinas were significantly broader than in either the mature ($p < 10^{-10}$) or the mature Cx36-KO EPSCs ($p < 10^{-17}$). There was no interaction between EPSC duration and contrast in either comparison. Error bars shown in (D), (E), (G), and (H) are standard deviation.

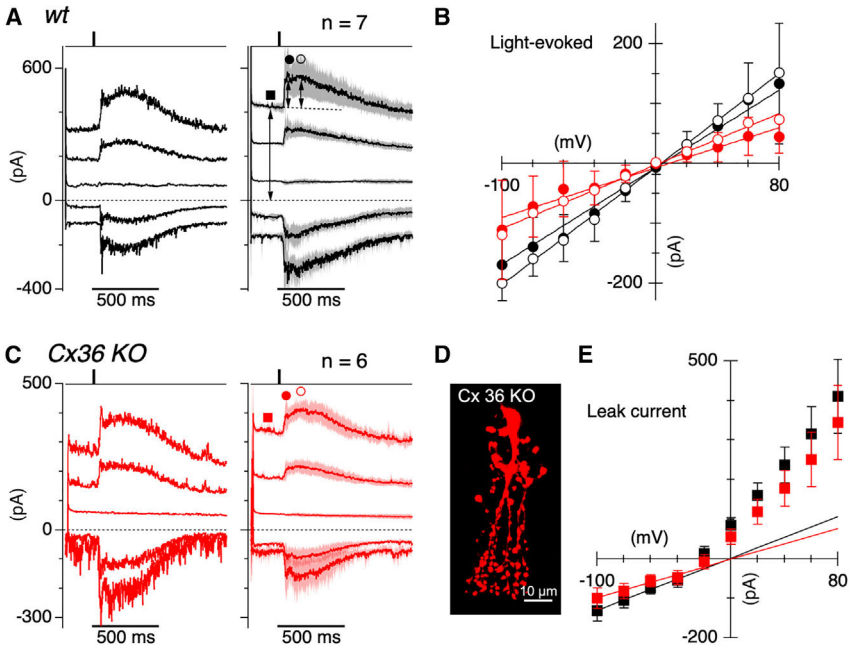

Figure 2. The current-voltage (I-V) relation of light-evoked inputs to AII-ACs

(A) Light-evoked postsynaptic currents (PSCs) at holding potentials of −80 to +80 mV in 40 mV increments. The left-hand traces show an example cell; the right-hand traces show averages from a group of cells (n = number of cells). Shading shows standard deviation. Stimulus timing is shown at the top. Double-headed arrows show the difference currents for the respective symbols in (B) and (E).

(B) Average I-V relations (mean ± SD) for the cells shown in (A) and (C). I-V relations for the net light-evoked EPSC were measured at the time points shown by the corresponding symbols in (A) and (C).

(C) Data for a group of Cx36-knockout (KO) retinas (P38). Format is the same as in (A).

(D) Confocal projection of a Cx36-KO mouse AII-AC. Alexa 488 was included in the patch pipette during the recording, and the morphology was reconstructed afterward.

(E) I-V relations for the leak current (time points shown in A and C). The slopes of the solid lines, which represent the input conductance over the normal physiological range, were 1.3 ± 1.2 nS for *wt* and 1.1 ± 0.3 nS for *Cx36*. The difference in slopes was not statistically significant ($p = 0.68$, $n = 6$, with non-pairwise t test). Error bars shown in (B) and (E) are standard deviation.

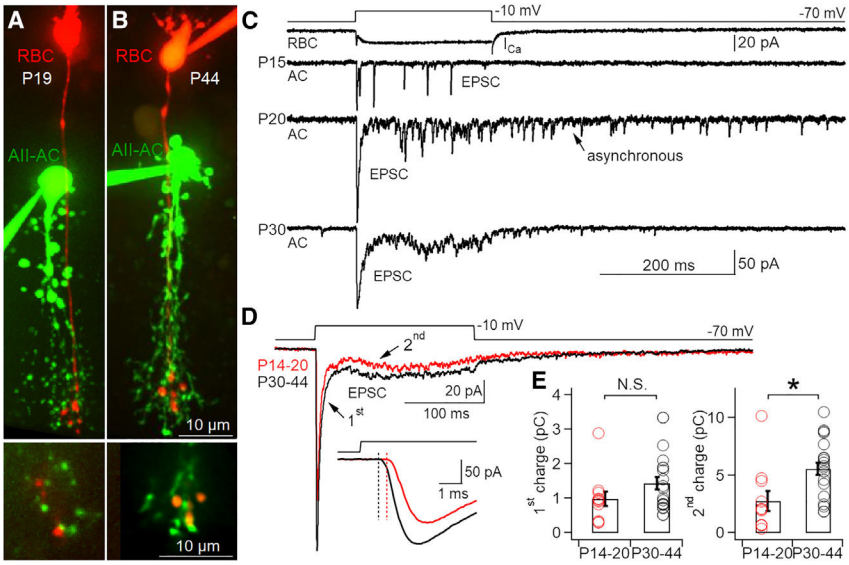

Figure 3. Maturation of evoked EPSCs at the RBC-to-AII-AC synapse

(A and B) Configuration of paired recordings between RBC and AII-AC in young (P19) and mature (P44) age groups. Alexa 488 (on the AII-AC, green) and 594 (on the RBC, red) were included at 50–100 µM in the patch pipette during recording. Images are maximum z projections taken with a spinning disk laser confocal microscope after recording. At the bottom are enlarged images from a single confocal plane. The overlapping green and red fluorescent signals indicate putative sites of synaptic contact. The scale bars (10 µm) shown in (B) are applicable to the horizontally aligned images in (A).

(C) Example of paired recordings at P15, P20, and P30. Depolarization of the presynaptic RBC soma from −70 to −10 mV for 200 ms resulted in an inward Ca^{2+} current (P20). The AII-AC soma was voltage clamped at −70 mV

(D) Averaged evoked EPSCs were compared between the recordings in young (n = 11) and more mature (n = 19) age groups. Peak (first; defined as the response within 30 ms of presynaptic depolarization) and slow sustained (second) current responses are shown in the averaged traces. The inset shows that onset delay is shorter in the more mature age group (black trace).

(E) The charge transfers for peak (first; p = 0.1219, Wilcoxon rank-sum test) and slow sustained (second; p = 0.005, Wilcoxon rank-sum test) current responses were compared in the two age groups (P14–P20, n = 11; P30–P44, n = 19). Note that the second charge is larger than the first by a factor of 2.5 for P14–P20 and a factor of 4 for P30–P44. Error bars indicate SEM.

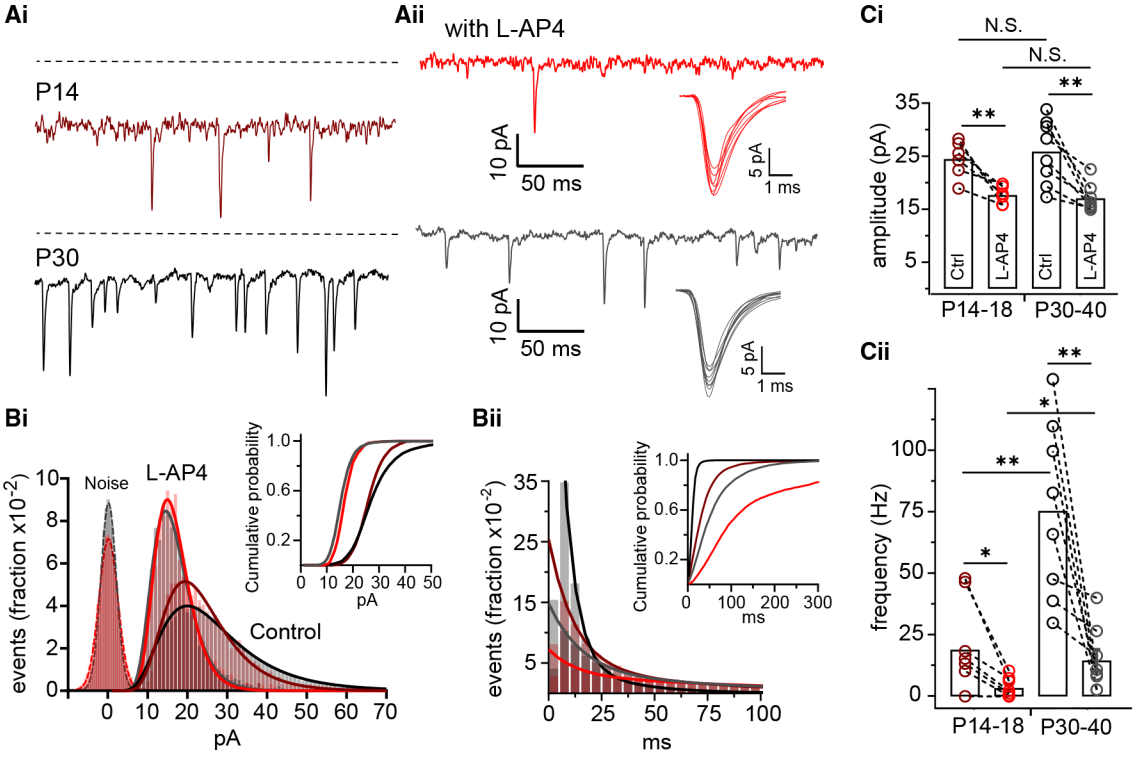

Figure 4. Maturation of spontaneous mEPSCs at the RBC-to-AII-AC synapse

(A) Representative recordings of mEPSCs in young (P14 example) and mature (P30 example) age groups before (control condition) (i) and after (ii) 10 μM L-AP4 application. Dotted lines in (i) in both traces (P14, P30) indicate that the baseline holding current changes after 10 μM L-AP4, for comparison. Insets show the averaged mEPSC waveforms for all individual cells (in the L-AP4 condition; n = 6 cells in the young and n = 8 cells in the mature group). AII-AC somas were clamped at −70 mV.

(B) (i) Amplitude distributions of mEPSCs in young (P14–P18, n = 6: control [brown-red], 19,868 events; L-AP4 [red], 9,306 events) and mature (P30–P40, n = 8: control (black), 54,487 events; L-AP4 (gray), 31,175 events) groups, fitted by log-normal curves. Noise (dashed Gaussians) is shown for the two age cohorts in the L-AP4 condition. Inset shows the corresponding cumulative probability distributions. (ii) Interevent interval distributions for the same datasets, fitted by double-exponential curves, and corresponding cumulative probability distributions (inset).

(C) (i) Average mEPSC amplitudes in young (P14–P18, n = 6) and mature (P30–P40, n = 8) age groups before (left) and after (right) L-AP4. (ii) Average mEPSC frequency for the same datasets with two additional cells in the young group (n = 8, total) that had frequencies below 0.1 Hz in control conditions. Data from these two cells were not included in (A), (B), or (Ci) due to insufficient number of mEPSCs.

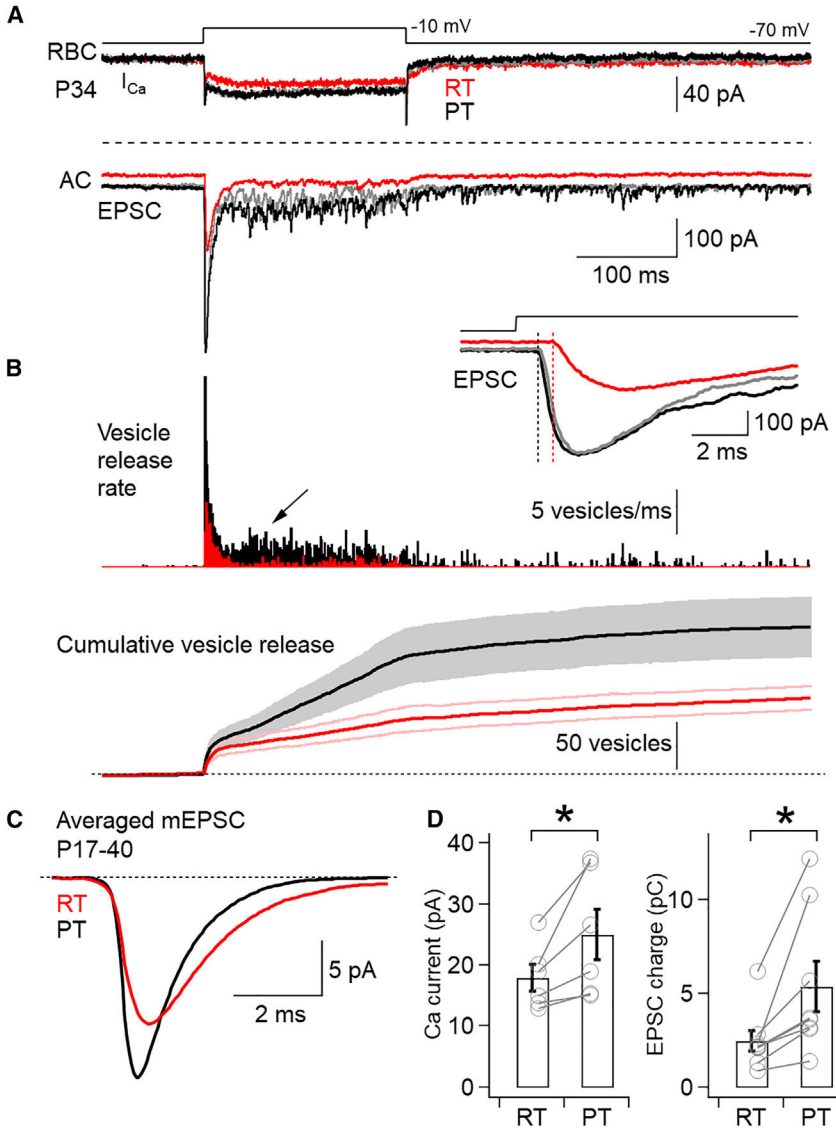

Figure 5. Temperature dependence of presynaptic Ca^{2+} currents and postsynaptic EPSCs

(A) Paired recordings were performed at room temperature (RT, 24°C) or at near physiological temperature (PT, 34°C). The temperature was initially set to PT (black), lowered to RT (red), and then raised back to PT (gray). Presynaptic Ca^{2+} currents and EPSC amplitudes were larger at PT compared with RT. Standing currents at −70 mV in AII-ACs became smaller at RT compared with PT. Dotted line indicates the zero current level.

(B) Instantaneous release rates and the integral of instantaneous release rates (i.e., cumulative vesicle releases) during step depolarization (n = 8, mean ± SEM, bottom) were calculated using deconvolution analysis (see method details in the STAR Methods). Note that the peak response, the slow sustained (second) response, and asynchronous releases were more prominent at PT (indicated by arrow). Onset delay was shorter at PT compared with RT (inset).

(C) Averaged mEPSC events are briefer at PT (black) than at RT (red). Because mEPSC amplitude and kinetics did not change with age, we show ages P17–P40 together.

(D) The size of presynaptic Ca^{2+} currents (n = 6; p = 0.0178 with pairwise t test) and the total EPSC charge (n = 8; p = 0.0337 with pairwise t test) are larger at PT than at RT for mice ages P17–P34 (*p < 0.05). Error bars indicate SEM.

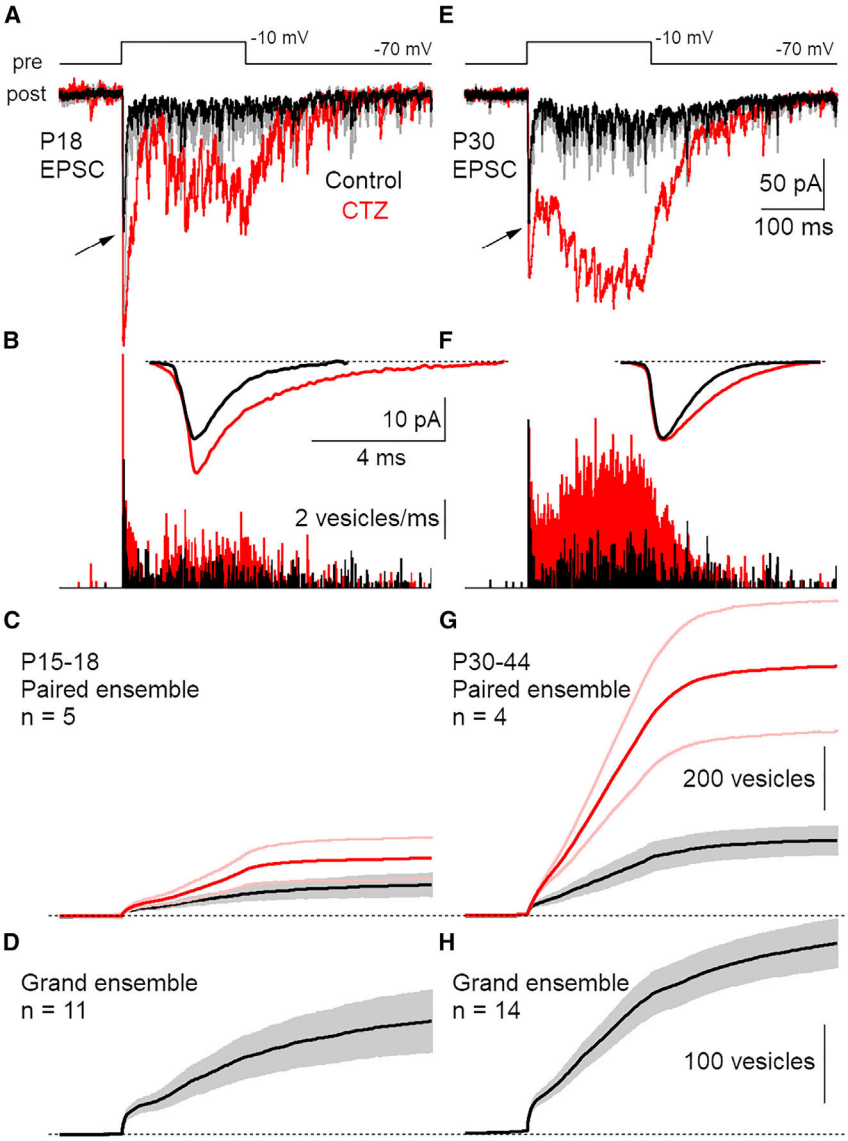

Figure 6. Presynaptic release kinetics in the presence of 50 μM cyclothiazide (CTZ; blocker of AMPAR desensitization) in young and mature age groups

(A and B) Evoked EPSCs and instantaneous release rate obtained via deconvolution analysis that uses the averaged mEPSC response (inset). Data are from a young mouse (P15–P18; n = 5). EPSCs in the absence (black) and presence (red) of CTZ are shown. Peak control response in the absence of CTZ was scaled to the response in the presence of CTZ (gray superimposed trace in A).

(C and G) The integrals of the instantaneous release rates (i.e., cumulative vesicle releases) during step depolarization were calculated with deconvolution in the absence (black, based on the mEPSCs in the inset in B) and presence of CTZ (red, based on the mEPSCs in the inset in B) and are shown for young (P15–P18; n = 5) and mature (P30–P44; n = 4) ages. The paired ensemble average with mean (black and red lines) ± SEM (gray shade and light red color indicated) value is shown.

(D and H) Total numbers of exocytosed vesicles were calculated by integrating the instantaneous release rate in all young (D; n = 11, P14–P20) and all mature (H; n = 14, P30–P44) age groups. The mean (black) ± SEM (gray shade indicated) values are displayed. (E and F) Same as in (A) and (B) for more mature mice (P30–P44; n = 4). Arrows in (A) and (E) indicate the initial peak EPSC of the control to compare the change in peak responses in the presence of CTZ. Spontaneous mEPSCs were averaged in the absence and presence of CTZ in both age groups (inset). The averaged mEPSCs were calculated from the sample number: control (n = 747, black) and CTZ (n = 248, red) in the young (inset in B) and control (n = 8,625, black) and CTZ (n = 8,699, red) in the mature age groups (inset in F).

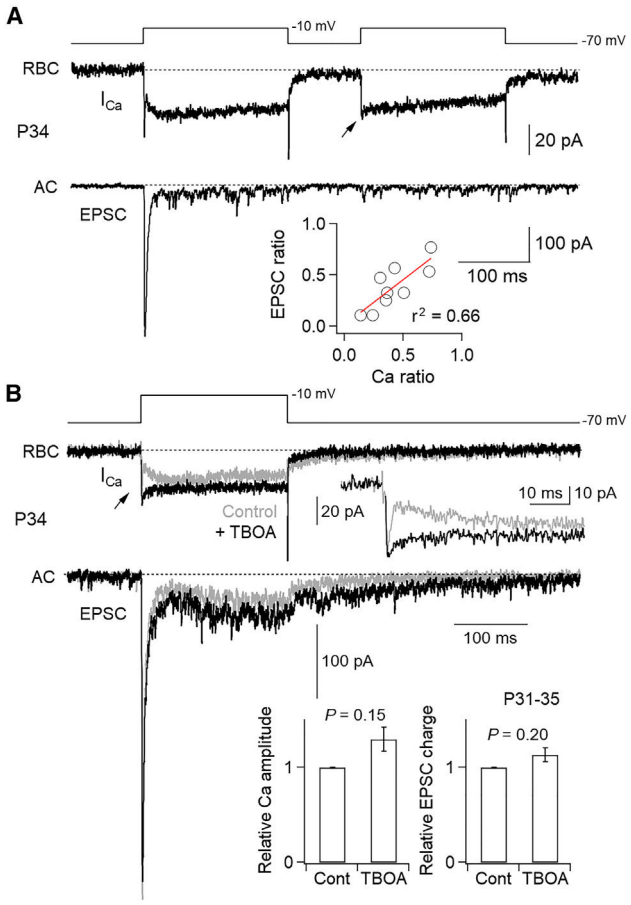

Figure 7. Blocking glutamate transporters on the RBC terminals does not significantly change the kinetics of EPSCs

(A) Paired-pulse protocol reveals the correlation between presynaptic glutamate-transporter-mediated currents on top of Ca^{2+} currents and EPSC sizes. The interval between two square pulses was 100 ms. Note that there is an initial notch on the Ca^{2+} currents elicited by the first pulse but not the second pulse (arrow), which did not elicit a large EPSC. The inset plots the paired-pulse ratio (stimulus duration, 200 ms; stimulation interval, 100 ms) for the relationship between initial notch size (defined by the difference between hump amplitude and steady-state current; second/first; Ca ratio) and EPSC peak size (second/first; EPSC ratio), indicating that there is a strong linear correlation (r^2 = 0.66). The data are from P16–P35.

(B) A selective antagonist of glutamate transporters, D,L-TBOA (100 μM), blocks the notch in the first Ca^{2+} current. Glutamate-transporter-mediated currents thus produce the notch. The leak current was subtracted in presynaptic Ca^{2+} current traces in each case (control in gray; TBOA in black). The inset shows the clear difference in the Ca^{2+} currents; however, the two components of the EPSC were not significantly altered by 100 μM D,L-TBOA (bottom). The average sizes of the steady-state Ca^{2+} currents (last 50 ms of Ca^{2+} current amplitude) and the corresponding EPSC charges were not significantly different (bottom inset; n = 4). Error bars indicate SEM. Also note the heterogeneity of the amplitudes of the

second sustained component of the EPSC for the synapses shown in (A) and (B), although they come from mice of the same age (P34).

KEY RESOURCES TABLE

REAGENT or RESOURCE	SOURCE	IDENTIFIER
Chemicals, peptides, and recombinant proteins		
Ames medium w/ L-glutamate	USBiologicals	A1372
Potassium methanesulfonate	Sigma-Aldrich	83000
Potassium chloride (KCl)	Sigma-Aldrich	P3911
Adenosine 5'-triphosphate (ATP) disodium salt hydrate	Sigma-Aldrich	A6419
Guanosine 5'-triphosphate (GTP) sodium salt hydrate	Sigma-Aldrich	G8877
Adenosine 5'-triphosphate (ATP) magnesium salt	Sigma-Aldrich	A9187
Ethyleneglycol- bis(β-aminoethyl)-N,N,N',N'-tetraacetic Acid (EGTA)	Sigma-Aldrich	324626
Tetraethylammonium chloride (TEA-Cl)	Sigma-Aldrich	T2265
Alexa 488 hydrazide	Invitrogen	A10436
Alexa 594 hydrazide	Invitrogen	A10438
Magnesium chloride ($MgCl_2$)	Sigma-Aldrich	M8266
4-(2-Hydroxyethyl)piperazine-1-ethanesulfonic acid (HEPES)	Sigma-Aldrich	H3375
Cs Gluconate	Prepared in house	
Cesium chloride (CsCl)	Sigma-Aldrich	C4036
Phosphocreatine di(tris) salt	Sigma-Aldrich	P1937
CsOH solution	Sigma-Aldrich	232041
L-AP4	Tocris	0103
Picrotoxin	Tocris	1128
TPMPA	Tocris	1040
Strychnine hydrochloride	Tocris	2785
Tetrodotoxin citrate (TTX)	Abcam	AB1200541MG
QX-314	Sigma-Aldrich	552233
IEM 1460	Tocris	1636
Cyclothiazide	Tocris	0713
D,L-TBOA	Tocris	1223
Cadmium chloride ($CdCl_2$)	Sigma-Aldrich	202908
D,L-AP5	Tocris	0105
Experimental models: Organisms/strains		
wild type mice	Jackson / Charles River Lab.	C57BL/6 strain
Cx36 knockout mice	In house	C57BL/6 background strain
Software and algorithms		
Igor Pro 8	Wavemetrics	RRID:SCR_000325

REAGENT or RESOURCE	SOURCE	IDENTIFIER
Prism 9	Graphpad	RRID:SCR_002798
Illustrator	Adobe	RRID:SCR_010279
MATLAB R2017a	MathWorks	RRID:SCR_001622
Other		
Resource website for the miniature EPSC detection	This paper	https://github.com/ADagostin/Igor-Procedures/tree/main/Procedures